DESY 01-097
July 2001

arXiv:hep-ex/0107052 v2 18 Oct 2001

Properties of hadronic final states in diffractive deep inelastic ep scattering at HERA

ZEUS Collaboration

Abstract

Characteristics of the hadronic final state of diffractive deep inelastic scattering events, $ep \to eXp$, were studied in the kinematic range $4 < M_X < 35$ GeV, $4 < Q^2 < 150$ GeV^2, $70 < W < 250$ GeV and $0.0003 < x_{\mathbb{P}} < 0.03$ with the ZEUS detector at HERA using an integrated luminosity of 13.8 pb^{-1}. The events were tagged by identifying the diffractively scattered proton using the leading proton spectrometer. The properties of the hadronic final state, X, were studied in its center-of-mass frame using thrust, thrust angle, sphericity, energy flow, transverse energy flow and "seagull" distributions. As the invariant mass of the system increases, the final state becomes more collimated, more aligned and more asymmetric in the average transverse momentum with respect to the direction of the virtual photon. Comparisons of the properties of the hadronic final state with predictions from various Monte Carlo model generators suggest that the final state is dominated by $q\bar{q}g$ states at the parton level.

The ZEUS Collaboration

S. Chekanov, M. Derrick, D. Krakauer, S. Magill, B. Musgrave, A. Pellegrino, J. Repond, R. Yoshida
Argonne National Laboratory, Argonne, Illinois 60439-4815

M.C.K. Mattingly
Andrews University, Berrien Springs, Michigan 49104-0380

P. Antonioli, G. Bari, M. Basile, L. Bellagamba, D. Boscherini[1], A. Bruni, G. Bruni, G. Cara Romeo, L. Cifarelli[2], F. Cindolo, A. Contin, M. Corradi, S. De Pasquale, P. Giusti, G. Iacobucci, G. Levi, A. Margotti, T. Massam, R. Nania, F. Palmonari, A. Pesci, G. Sartorelli, A. Zichichi
University and INFN Bologna, Bologna, Italy

G. Aghuzumtsyan, I. Brock, S. Goers, H. Hartmann, E. Hilger, P. Irrgang, H.-P. Jakob, A. Kappes[3], U.F. Katz[4], R. Kerger, O. Kind, E. Paul, J. Rautenberg, H. Schnurbusch, A. Stifutkin, J. Tandler, K.C. Voss, A. Weber, H. Wieber
Physikalisches Institut der Universität Bonn, Bonn, Germany

D.S. Bailey[5], N.H. Brook[5], J.E. Cole, B. Foster G.P. Heath, H.F. Heath, S. Robins, E. Rodrigues[6], J. Scott, R.J. Tapper, M. Wing
H.H. Wills Physics Laboratory, University of Bristol, Bristol, United Kingdom

M. Capua, A. Mastroberardino, M. Schioppa, G. Susinno
Calabria University, Physics Department and INFN, Cosenza, Italy [e]

H.Y. Jeoung, J.Y. Kim, J.H. Lee, I.T. Lim, K.J. Ma, M.Y. Pac[7]
Chonnam National University, Kwangju, Korea

A. Caldwell, M. Helbich, W. Liu, X. Liu, B. Mellado, S. Paganis, S. Sampson, W.B. Schmidke, F. Sciulli
Nevis Laboratories, Columbia University, Irvington on Hudson, New York 10027 [o]

J. Chwastowski, A. Eskreys, J. Figiel, K. Klimek[8], K. Olkiewicz, M.B. Przybycień[9], P. Stopa, L. Zawiejski
Institute of Nuclear Physics, Cracow, Poland

B. Bednarek, I. Grabowska-Bold, K. Jeleń, D. Kisielewska, A.M. Kowal[10], M. Kowal, T. Kowalski, B. Mindur, M. Przybycień, E. Rulikowska-Zarębska, L. Suszycki, D. Szuba, J. Szuba
Faculty of Physics and Nuclear Techniques, University of Mining and Metallurgy, Cracow, Poland

A. Kotański
Department of Physics, Jagellonian University, Cracow, Poland

L.A.T. Bauerdick[11], U. Behrens, K. Borras, V. Chiochia, J. Crittenden[12], D. Dannheim, K. Desler, G. Drews, A. Fox-Murphy, U. Fricke, A. Geiser, F. Goebel, P. Göttlicher, R. Graciani, T. Haas, W. Hain, G.F. Hartner, K. Hebbel, S. Hillert, W. Koch[13]†, U. Kötz, H. Kowalski, H. Labes, B. Löhr, R. Mankel, J. Martens, M. Martínez, M. Milite, M. Moritz, D. Notz, M.C. Petrucci, A. Polini, U. Schneekloth, F. Selonke, S. Stonjek, G. Wolf, U. Wollmer, J.J. Whitmore[14], R. Wichmann[15], C. Youngman, W. Zeuner
Deutsches Elektronen-Synchrotron DESY, Hamburg, Germany

C. Coldewey, A. Lopez-Duran Viani, A. Meyer, S. Schlenstedt
DESY Zeuthen, Zeuthen, Germany

G. Barbagli, E. Gallo, P. G. Pelfer
University and INFN, Florence, Italy

A. Bamberger, A. Benen, N. Coppola, P. Markun, H. Raach[16], S. Wölfle
Fakultät für Physik der Universität Freiburg i.Br., Freiburg i.Br., Germany

M. Bell, P.J. Bussey, A.T. Doyle, C. Glasman, S.W. Lee[17], A. Lupi, G.J. McCance, D.H. Saxon, I.O. Skillicorn
Department of Physics and Astronomy, University of Glasgow, Glasgow, United Kingdom

B. Bodmann, N. Gendner, U. Holm, H. Salehi, K. Wick, A. Yildirim, A. Ziegler
Hamburg University, I. Institute of Exp. Physics, Hamburg, Germany

T. Carli, A. Garfagnini, I. Gialas[18], E. Lohrmann
Hamburg University, II. Institute of Exp. Physics, Hamburg, Germany

C. Foudas, R. Gonçalo[6], K.R. Long, F. Metlica, D.B. Miller, A.D. Tapper, R. Walker
Imperial College London, High Energy Nuclear Physics Group, London, United Kingdom

P. Cloth, D. Filges
Forschungszentrum Jülich, Institut für Kernphysik, Jülich, Germany

M. Kuze, K. Nagano, K. Tokushuku[19], S. Yamada, Y. Yamazaki
Institute of Particle and Nuclear Studies, KEK, Tsukuba, Japan

A.N. Barakbaev, E.G. Boos, N.S. Pokrovskiy, B.O. Zhautykov
Institute of Physics and Technology of Ministry of Education and Science of Kazakhstan, Almaty, Kazakhstan

S.H. Ahn, S.B. Lee, S.K. Park
Korea University, Seoul, Korea

H. Lim[17], D. Son
Kyungpook National University, Taegu, Korea

F. Barreiro, G. García, O. González, L. Labarga, J. del Peso, I. Redondo[20], J. Terrón, M. Vázquez
Depto de Física Teórica, Universidad Autónoma Madrid, Madrid, Spain

M. Barbi, A. Bertolin, F. Corriveau, A. Ochs, S. Padhi, D.G. Stairs
Department of Physics, McGill University, Montréal, Québec, Canada H3A 2T8

T. Tsurugai
Meiji Gakuin University, Faculty of General Education, Yokohama, Japan

A. Antonov, V. Bashkirov[21], P. Danilov, B.A. Dolgoshein, D. Gladkov, V. Sosnovtsev, S. Suchkov
Moscow Engineering Physics Institute, Moscow, Russia

R.K. Dementiev, P.F. Ermolov, Yu.A. Golubkov, I.I. Katkov, L.A. Khein, N.A. Korotkova, I.A. Korzhavina, V.A. Kuzmin, B.B. Levchenko, O.Yu. Lukina, A.S. Proskuryakov, L.M. Shcheglova, A.N. Solomin, N.N. Vlasov, S.A. Zotkin
Moscow State University, Institute of Nuclear Physics, Moscow, Russia

C. Bokel, J. Engelen, S. Grijpink, E. Maddox, E. Koffeman, P. Kooijman, S. Schagen, E. Tassi, H. Tiecke, N. Tuning, J.J. Velthuis, L. Wiggers, E. de Wolf
NIKHEF and University of Amsterdam, Amsterdam, Netherlands

N. Brümmer, B. Bylsma, L.S. Durkin, J. Gilmore, C.M. Ginsburg, C.L. Kim, T.Y. Ling
Physics Department, Ohio State University, Columbus, Ohio 43210

S. Boogert, A.M. Cooper-Sarkar, R.C.E. Devenish, J. Ferrando, J. Große-Knetter[22], T. Matsushita, M. Rigby, O. Ruske[23], M.R. Sutton, R. Walczak
Department of Physics, University of Oxford, Oxford United Kingdom

R. Brugnera, R. Carlin, F. Dal Corso, S. Dusini, S. Limentani, A. Longhin, A. Parenti, M. Posocco, L. Stanco, M. Turcato
Dipartimento di Fisica dell' Università and INFN, Padova, Italy

L. Adamczyk[24], L. Iannotti[24], B.Y. Oh, P.R.B. Saull[24], W.S. Toothacker[13]†
Department of Physics, Pennsylvania State University, University Park, Pennsylvania 16802

Y. Iga
Polytechnic University, Sagamihara, Japan

G. D'Agostini, G. Marini, A. Nigro
Dipartimento di Fisica, Università 'La Sapienza' and INFN, Rome, Italy

C. Cormack, J.C. Hart, N.A. McCubbin
Rutherford Appleton Laboratory, Chilton, Didcot, Oxon, United Kingdom

D. Epperson, C. Heusch, H. Sadrozinski, A. Seiden, D.C. Williams
University of California, Santa Cruz, California 95064 [n]

I.H. Park
Seoul National University, Seoul, Korea

N. Pavel
Fachbereich Physik der Universität-Gesamthochschule Siegen, Germany

H. Abramowicz, S. Dagan, A. Gabareen, S. Kananov, A. Kreisel, A. Levy
Raymond and Beverly Sackler Faculty of Exact Sciences, School of Physics, Tel-Aviv University, Tel-Aviv, Israel

T. Abe, T. Fusayasu, T. Kohno, K. Umemori, T. Yamashita
Department of Physics, University of Tokyo, Tokyo, Japan

R. Hamatsu, T. Hirose, M. Inuzuka, S. Kitamura[25], K. Matsuzawa, T. Nishimura
Tokyo Metropolitan University, Deptartment of Physics, Tokyo, Japan

M. Arneodo[26], N. Cartiglia, R. Cirio, M. Costa, M.I. Ferrero, S. Maselli, V. Monaco, C. Peroni, M. Ruspa, R. Sacchi, A. Solano, A. Staiano
Università di Torino, Dipartimento di Fisica Sperimentale and INFN, Torino, Italy

D.C. Bailey, C.-P. Fagerstroem, R. Galea, T. Koop, G.M. Levman, J.F. Martin, A. Mirea, A. Sabetfakhri
Department of Physics, University of Toronto, Toronto, Ontario, Canada M5S 1A7

J.M. Butterworth, C. Gwenlan, R. Hall-Wilton, M.E. Hayes[22], E.A. Heaphy, T.W. Jones, J.B. Lane, M.S. Lightwood, B.J. West
Physics and Astronomy Department, University College London, London, United Kingdom

J. Ciborowski[27], R. Ciesielski, G. Grzelak, R.J. Nowak, J.M. Pawlak, B. Smalska[28], T. Tymieniecka[29], A. Ukleja[29], J. Ukleja, J.A. Zakrzewski, A.F. Żarnecki
Warsaw University, Institute of Experimental Physics, Warsaw, Poland

M. Adamus, P. Plucinski, J. Sztuk
Institute for Nuclear Studies, Warsaw, Poland

Y. Eisenberg, L.K. Gladilin[30], D. Hochman, U. Karshon
Department of Particle Physics, Weizmann Institute, Rehovot, Israel

J. Breitweg, D. Chapin, R. Cross, D. Kçira, S. Lammers, D.D. Reeder, A.A. Savin, W.H. Smith
Department of Physics, University of Wisconsin, Madison, Wisconsin 53706

A. Deshpande, S. Dhawan, V.W. Hughes P.B. Straub
Department of Physics, Yale University, New Haven, Connecticut 06520-8121

S. Bhadra, C.D. Catterall, W.R. Frisken, M. Khakzad, S. Menary
Department of Physics, York University, Ontario, Canada M3J 1P3

[1] now visiting scientist at DESY
[2] now at Univ. of Salerno and INFN Napoli, Italy
[3] supported by the GIF, contract I-523-13.7/97
[4] on leave of absence at University of Erlangen-Nürnberg, Germany
[5] PPARC Advanced fellow
[6] supported by the Portuguese Foundation for Science and Technology (FCT)
[7] now at Dongshin University, Naju, Korea
[8] supported by the Polish State Committee for Scientific Research, grant no. 5 P-03B 08720
[9] now at Northwestern Univ., Evaston/IL, USA
[10] supported by the Polish State Committee for Scientific Research, grant no. 5 P-03B 13720
[11] now at Fermilab, Batavia/IL, USA
[12] on leave of absence from Bonn University
[13] deceased
[14] on leave from Penn State University, USA
[15] partly supported by Penn State University and GIF, contract I-523-013.07/97
[16] supported by DESY
[17] partly supported by an ICSC-World Laboratory Björn H. Wiik Scholarship
[18] Univ. of the Aegean, Greece
[19] also at University of Tokyo
[20] supported by the Comunidad Autonoma de Madrid
[21] now at Loma Linda University, Loma Linda, CA, USA
[22] now at CERN, Geneva, Switzerland
[23] now at IBM Global Services, Frankfurt/Main, Germany
[24] partly supported by Tel Aviv University
[25] present address: Tokyo Metropolitan University of Health Sciences, Tokyo 116-8551, Japan
[26] now also at Università del Piemonte Orientale, I-28100 Novara, Italy
[27] and Łódź University, Poland
[28] supported by the Polish State Committee for Scientific Research, grant no. 2 P-03B 00219
[29] supported by the Polish State Committee for Scientific Research, grant no. 5 P-03B 09820
[30] on leave from MSU, partly supported by University of Wisconsin via the U.S.-Israel BSF

1 Introduction

A class of deep inelastic scattering (DIS) events has been observed at HERA that have the characteristics of diffractive interactions. These events have a large rapidity gap [1] between the recoil-proton system and the produced hadronic system, and a small momentum transfer to the proton [2]. The events can be pictured in terms of the t-channel exchange of an object that carries the quantum numbers of the vacuum, called the Pomeron ($\mathbb{P}$), see Fig. 1(a). However, the nature of the Pomeron in DIS is at present far from clear. Measurements by the H1 [3, 4, 5] and ZEUS [6] collaborations have shown that, in QCD-inspired models of the diffractive process, the Pomeron can be described as an object whose partonic composition is dominated by gluons. Alternatively, the diffractive process can be described by the dissociation of the virtual photon into a $q\bar{q}$ or $q\bar{q}g$ final state that interacts with the proton by the exchange of a gluon ladder [7].

The study of the hadronic final state in e^+e^- annihilation [8] has been a powerful tool in gaining information about the underlying partonic state. Similarly, the study of the partonic content of the hadronic final state in diffraction is a natural way to explore the dynamics of diffraction.

In this paper, a study is reported of the hadronic system, X, produced in the DIS process $ep \to eXp$, where the diffractively scattered proton stays intact. The proton was detected and its three-momentum measured in the leading proton spectrometer (LPS) [9]. Diffractive events are defined, for the purpose of this paper, as those events which contain a proton with more than 97% of the initial proton beam energy. Previous results on hadronic final states in diffractive events at HERA have been obtained with the requirement of a large rapidity gap between the observed hadronic system and the scattered proton [10, 11]. The results obtained with rapidity-gap events were either defined in a reduced phase space by imposing a cut in rapidity [10, 12], or Monte Carlo simulated events were used to extrapolate the characteristics of diffractive events over the areas of phase space removed by the rapidity-gap cut [11]. By using the scattered proton to tag diffractive events, there is no need to rely on Monte Carlo generators to model correctly the part of the final state removed by the rapidity cuts, and the full angular coverage of the central detector can be used.

The properties of the hadronic system, X, were studied in terms of global event-shape variables such as thrust and sphericity in the center-of-mass (CMS) frame of X. This is analogous to the studies of global event-shape variables in e^+e^- annihilation [8] as a function of the CMS energy and to the analysis that led to the interpretation of three-jet events in terms of gluon bremsstrahlung [13]. In addition to global event-shape variables, the properties of the diffractive events were described in terms of inclusive distributions such as energy flow.

2 Experimental setup

The data were recorded in 1997 with the ZEUS detector and correspond to an integrated luminosity of 13.8 ± 0.3 pb^{-1}. A detailed description of the ZEUS detector can be found elsewhere [14]. A brief outline of the main detector components most relevant for this analysis is given below. Charged particles are tracked by the central tracking detector (CTD) [15], which operates in a magnetic field of 1.43 T provided by a thin superconducting coil. The CTD consists of 72 cylindrical drift chamber layers, organized in 9 superlayers covering the polar angle[1] region $15° < \theta < 164°$. The transverse-momentum resolution for full-length tracks is $\sigma(p_T)/p_T = 0.0058 p_T \oplus 0.0065 \oplus 0.0014/p_T$, with p_T in GeV. The high-resolution uranium-scintillator calorimeter (CAL) [16] consists of three parts: the forward (FCAL), the barrel (BCAL) and the rear (RCAL) calorimeters. Each part is subdivided transversely into towers and longitudinally into one electromagnetic section (EMC) and either one (in RCAL) or two (in BCAL and FCAL) hadronic sections (HAC). The smallest subdivision of the calorimeter is called a cell. The CAL energy resolutions, as measured under test beam conditions, are $\sigma(E)/E = 0.18/\sqrt{E}$ for electrons and $\sigma(E)/E = 0.35/\sqrt{E}$ for hadrons (E in GeV).

The LPS [9] detects charged particles scattered at small angles and carrying a substantial fraction of the incoming proton momentum; these particles remain in the beampipe and their trajectory is measured by a system of position-sensitive silicon micro-strip detectors very close to the proton beam. The track deflection induced by the magnets in the proton beamline is used for the momentum analysis of the scattered proton. The LPS consists of six detector stations, S1 to S6, placed along the beamline in the direction of the outgoing protons, at $Z = 23.8$ m, 40.3 m, 44.5 m, 63.0 m, 81.2 m and 90.0 m from the interaction point, respectively. In this analysis, only the stations S4 to S6 were used. These stations consist of two halves, each equipped with an assembly of six parallel planes of silicon micro-strip detectors which can be inserted to a position near the proton beam. Each detector plane has an elliptical cutout which follows the profile of the 10σ envelope of the beam, where σ is the standard deviation of the spatial distribution of the beam in the transverse plane. The acceptance of stations S4 to S6 of the LPS for protons close to the beam energy is a few per cent and approximately uniform for $0.075 < |t| < 0.35$ GeV^2. The LPS longitudinal momentum resolution is $\sigma(p_Z)/p_Z = 5 \times 10^{-6} p_Z$ (p_Z in GeV). The transverse momentum resolutions, dominated by the proton beam emittance, are $\sigma_{p_X} = 35$ MeV and $\sigma_{p_Y} = 90$ MeV.

[1] The ZEUS coordinate system is a right-handed Cartesian system, with the Z axis pointing in the proton beam direction, referred to as the "forward direction", and the X axis pointing left towards the center of HERA. The coordinate origin is at the nominal interaction point. The pseudorapidity is defined as $\eta = -\ln\left(\tan\frac{\theta}{2}\right)$, where the polar angle, θ, is measured with respect to the proton beam direction.

3 Kinematic variables and event reconstruction

3.1 Kinematic variables

The event kinematics of DIS processes can be described by the negative squared four-momentum transfer at the lepton vertex, $Q^2 = -q^2 = -(k - k')^2$ (k and k' denote the four-momenta of the initial- and final-state positrons, respectively), and the Bjorken scaling variable, $x = Q^2/(2P \cdot q)$, where P is the four-momentum of the proton. The fraction of the energy transferred to the proton in its rest frame, y, is related to these two variables by $y = P \cdot q/(P \cdot k) \simeq Q^2/xs$, where $\sqrt{s}$ is the positron-proton CMS energy. The CMS energy of the $\gamma^* p$ system, W, is given by $W^2 = (q + P)^2 = Q^2(1 - x)/x + M_p^2$, where M_p denotes the proton mass. Unless otherwise noted, the double angle method [17] is used to reconstruct the kinematic variables from the measured quantities.

Two more kinematic variables are needed to describe a diffractive DIS event, $e(k) + p(P) \rightarrow e'(k') + X + p'(P')$, where the scattered proton, p', has four-momentum $P' = (E_{p'}, P'_X, P'_Y, P'_Z)$. The squared four-momentum transfer at the proton vertex is given by

$$t = (P - P')^2 \simeq -P_T^2,$$

where $P_T^2 = P_X'^2 + P_Y'^2$, and the fraction of the beam momentum retained by the final proton is

$$x_L = \frac{|\boldsymbol{P}'|}{|\boldsymbol{P}|} \simeq \frac{E_{p'}}{E_p},$$

where $E_p = 820$ GeV denotes the incident proton beam energy. Both t and x_L are measured with the LPS. Other useful variables in diffractive DIS are:

$$x_{I\!P} = \frac{(P - P') \cdot q}{P \cdot q} = \frac{M_X^2 + Q^2 - t}{W^2 + Q^2 - M_p^2} \simeq 1 - x_L$$

and

$$\beta = \frac{Q^2}{2(P - P') \cdot q} = \frac{x}{x_{I\!P}} \simeq \frac{Q^2}{M_X^2 + Q^2},$$

where M_X is the invariant mass of the final-state, X, determined as described below. In the Pomeron-exchange picture, $x_{I\!P}$ is the fraction of the proton's momentum carried by the Pomeron. For a Pomeron with partonic constituents, β is then the fraction of the Pomeron's momentum carried by the parton that absorbs the virtual photon.

3.2 Reconstruction of M_X

Two methods were used in this analysis to determine the invariant mass of the system X. The first method measured the mass directly from X. The individual objects belonging

to X were reconstructed by combining charged tracks measured in the CTD and neutral energy clusters measured in the calorimeter into energy flow objects (EFOs [6]). In this procedure, the tracks and clusters associated with the scattered positron were not used. The four-vectors of the EFOs were calculated assuming the pion mass. The invariant mass can then be reconstructed using these four-momenta as

$$M^2_{X,EFO} = (\sum_i E_i)^2 - (\sum_i P_{Xi})^2 - (\sum_i P_{Yi})^2 - (\sum_i P_{Zi})^2. \quad (1)$$

The second method inferred M_X from the measurement of the final-state proton and the scattered positron, which enter into the reconstruction of the kinematic variables x and y via the double angle method. M^2_X is then given by

$$M^2_{X,LPS} = sy(1 - x_L - x). \quad (2)$$

Since the LPS method has better resolution at higher values of M_X and the EFO measurement is better at lower values, M_X was evaluated as the weighted average of the values obtained with the two methods. Before combining the two M_X values, correction factors obtained from Monte Carlo studies were applied. This resulted in a resolution on M_X of about 25% at low M_X, improving to 15% at high M_X.

3.3 Boost into the $\gamma^*\mathbb{P}$ center-of-mass system

The boost into the CMS of X ($\gamma^*\mathbb{P}$), Fig. 1(b), was determined from the four-momenta of the γ^* and $\mathbb{P}$. The γ^* four-momentum was calculated from the energy and angles of the scattered positron. The best reconstruction of the $\mathbb{P}$ four-momentum was obtained by combining the information from the LPS and the ZEUS main detector. The X and Y components of the $\mathbb{P}$ four-momentum were taken to be equal to the negative of the X and Y momentum components of the scattered proton measured with the LPS. The Z component was taken to be the total P_Z of all EFOs ($P_Z^{tot} = \sum_i P_{Zi}$) minus the Z component of the γ^* four-momentum. Finally, the energy component was calculated by requiring that the $\gamma^*\mathbb{P}$ invariant mass be equal to the value of M_X determined by the combination of the information from the LPS and the EFOs, as described earlier.

The resolution on the angle between the $\gamma^*\mathbb{P}$ axis and the ZEUS Z-axis, as estimated by Monte Carlo studies, was approximately inversely proportional to M_X and equal to 10 mrad at $M_X = 20$ GeV. An improvement in the accuracy of the measurement by a factor of three was achieved using the LPS compared to a measurement without its use, i.e. substituting $p_X = p_Y = 0$.

4 Event selection

Deep inelastic scattering events were selected in a manner similar to those of the ZEUS F_2 analysis [18] by requiring:

- the presence of a fully contained and isolated positron with energy greater than 10 GeV and matched to a charged track, if within the acceptance of the CTD;
- a value of y greater than 0.05, evaluated using the Jacquet-Blondel method [19];
- a value of $\delta = E^{tot} - P_Z^{tot}$ in the range $40 < \delta < 65$ GeV, where E^{tot} and $\boldsymbol{P^{tot}}$ are, respectively, the total energy and momentum of the event in the main detector, including the scattered positron;
- the Z coordinate of the event vertex within 50 cm of the nominal interaction point.

Diffractive events were then selected by requiring a well reconstructed LPS track [9] carrying more than 95% of the beam energy ($x_L > 0.95$). The LPS track was required to pass no closer than 0.04 cm to the HERA beampipe, and the quantity $\delta^+ = E^{tot} + P_Z^{tot} + 2E_p x_L$ was required to be less than $2E_p + 20$ GeV to be consistent with longitudinal momentum conservation after taking the LPS resolution into account. Since the results presented here were found to be independent of t, no explicit cut on t was applied.

To provide a sample for which the acceptance is large and uniform, to remove events measured with low resolution and to reject events corresponding to exclusive production of vector mesons, the following kinematic cuts were applied:

- $70 < W < 250$ GeV;
- $0.0003 < x_{I\!P} < 0.03$;
- $4 < Q^2 < 150$ GeV^2;
- $4 < M_X < 35$ GeV.

In addition, at least four EFOs in the system X were required. These cuts define the kinematic range for all results presented in this paper, unless otherwise noted. The final data sample contained 2355 events.

5 Models of the diffractive final state

The data were compared with three Monte Carlo generators based on different theoretical models. For all generators, hadronization was simulated using the Lund string model as implemented in JETSET 7.4 [20]. The models considered here produce either a $q\bar{q}$ pair or a $q\bar{q}g$ final state at the parton level. However, the dynamics of the production of these states is different for each model, thus yielding predictions that differ in their relative contributions of $q\bar{q}$ and $q\bar{q}g$ states, as well as in the final-state topology. Common to all three models is that the $q\bar{q}g$-type events dominate the final state at high masses. In such events, the gluon usually travels in the direction of the Pomeron.

5.1 Resolved Pomeron model

In the resolved Pomeron approach [21], the exchanged particle is assumed to have a partonic structure consisting of quarks and gluons. A sample of resolved Pomeron events was produced with the RAPGAP 2.08/06 generator [22]. The hadronic final state is simulated in analogy to ordinary DIS. The Pomeron parton density functions (PDFs) used were those determined by the H1 collaboration from their measurement of $d^3\sigma/dx_{I\!P}dQ^2d\beta$ [3].

When the virtual photon in a diffractive event interacts with a quark in the Pomeron, the lowest-order final state is a $q\bar{q}$. At $\mathcal{O}(\alpha_s)$, $q\bar{q}g$ final states can be produced by the radiation of an extra gluon via the QCD-Compton (QCDC) process. In addition, $q\bar{q}g$ final states are produced via the boson-gluon fusion (BGF) process between the virtual photon and a gluon in the Pomeron. The Pomeron remnant consists of a quark in the $q\bar{q}$ and QCDC events and of a gluon in BGF events. Additional parton radiation from the remnant partons is suppressed. The following RAPGAP options were used:

- the leading-order version of the H1 Fit 2 was used. In the fit, more than 80 % of the Pomeron momentum is carried by the gluons.
- the final-state parton system in $q\bar{q}$-type events was simulated with limited transverse momentum with respect to the $\gamma^*I\!P$ axis (intrinsic transverse momentum, k_T), randomly distributed according to $\exp(-5.5k_T^2)$ (k_T in GeV);
- to avoid divergences in the matrix elements for the $\mathcal{O}(\alpha_s)$ processes for massless quarks, the transverse momentum squared of any outgoing parton was required to be larger than 3 GeV^2;
- higher-order QCD radiation was simulated using initial- and final-state parton showers (MEPS) [23];

- the generator was run for light flavors and charm production (produced via the BGF process) separately, and the final sample was obtained by mixing the two according to their relative cross sections as predicted by RAPGAP.

The curves corresponding to this model are labeled "RG resolved $\mathbb{P}$" in later figures. The model labeled "RG $q\bar{q}$ part only" in later figures was obtained by selecting events from the above sample that were not produced via the BGF process.

5.2 Photon dissociative model

In the rest frame of the proton, diffractive scattering can be viewed as the dissociation of the virtual photon into a $q\bar{q}$ pair (Fig. 1(c)) well before the interaction with the proton. For higher masses, the $q\bar{q}g$ final state (Fig. 1(d)) becomes important. The dissociated photon system couples to the proton by color-singlet exchange.

The simplest realization of this color singlet is the exchange of two gluons with opposite color charge (two-gluon exchange model). The RIDI2.0 program [24] implements a two-gluon model following the approach of Ryskin [25], where the diffractive dissociation is treated in the framework of the leading log approximation (LLA) of perturbative QCD. The cross section is proportional to the square of the gluon density of the proton, which was taken from the CTEQ4M [26] parameterization of the proton structure function with an appropriately chosen cut-off parameter for the transverse momentum of the final-state gluon. The contributions of both transversely and longitudinally polarized photons are included. A large theoretical uncertainty in the relative contributions of $q\bar{q}$ and $q\bar{q}g$ states remains. This uncertainty is reflected in the wide range allowed for the (α_s-dependent) k-factors, which determine the relative cross sections of the $q\bar{q}$ and $q\bar{q}g$ contributions.

Another model based on photon dissociation is that of Golec-Biernat and Wüsthoff [27], in which the virtual photon splits into a $q\bar{q}$ or $q\bar{q}g$ color dipole. The interaction of this dipole with the proton can be described by an effective dipole cross section taking the dynamics of saturation into account. The dipole cross section was parameterized using the HERA measurements of the DIS total cross section between $Q^2 = 0.1$ GeV^2 and $Q^2 = 100$ GeV^2. The production of $q\bar{q}$ and $q\bar{q}g$ final states is calculated using these parameters. The relative contribution of $q\bar{q}$ and $q\bar{q}g$ events is fixed by QCD color factors. This model is implemented in the SATRAP Monte Carlo generator [28] which uses the additional approximation of strong ordering in the transverse momenta: $k_T(g) \ll k_T(q, \bar{q})$. In the course of the ZEUS analysis of diffractive 3-jet events [29], it was found that the modeling of higher-order QCD processes was inadequately implemented in SATRAP. Most notably, no initial-state parton cascades were included, and the final-state QCD radiation from the gluon in the dominant $q\bar{q}g$ contribution was suppressed. A new implementation of

higher-order QCD processes in SATRAP was carried out [30, 31], in which the color-dipole model (CDM) was implemented in a similar fashion to that in RAPGAP. This model is referred to as SATRAP-CDM.

5.3 JETSET

If the diffractive DIS hadronic system, X, is produced by a virtual photon splitting into a $q\bar{q}$ pair, its properties would be expected to be similar to those of the hadronic system produced by e^+e^- annihilation at a CMS energy $\sqrt{s} = M_X$. The e^+e^- final state, as simulated by the JETSET program [20], was used as a baseline to which both the data and the diffractive Monte Carlo generators were compared. JETSET is known to describe accurately many details of the final state in e^+e^- collisions.

6 Data correction and background

Monte Carlo simulations were used to correct the data for the resolution and acceptance of the main detector and the LPS, and to estimate the size and influence of the background. To estimate the model dependence of these corrections, two different generators were used: RAPGAP [22] and RIDI [24]. RAPGAP events were generated with the H1 QCD Fit 2 [3] for the $I\!P$ structure function, as described in Section 5.1, except that CDM rather then MEPS was used for higher-order initial- and final-state QCD radiation. This model gives a poor description of the hadronic final state as well as of some kinematic variables as measured at the detector level. To obtain a sample which gives a good description of all observed distributions, the RAPGAP generator was reweighted to reproduce the data. The corresponding distributions are labeled "mod. RG" in Figs. 2 to 5. A similar reweighting procedure was carried out for RIDI. Both samples were passed through a GEANT 3.13 [32] simulation of the ZEUS detector, subjected to the same trigger requirements as the data and processed by the same reconstruction programs.

In addition, changes in the HERA beamline parameters during the running period and the finite resolution of the motors that determine the position of the LPS, neither of which was simulated in the Monte Carlo, were taken into account by reweighting and smearing the simulated x_L distribution.

The primary source of background in this analysis is the accidental overlap of a DIS event with an unrelated beam-halo proton measured in the LPS. This contribution was assumed to be constant over the running period. To estimate its size, a sample of such background events was studied. Background protons were identified by selecting DIS events with $E^{tot} + P_Z^{tot} > 100$ GeV (using only CAL) and an LPS track with $x_L > 0.9$. From energy

conservation allowing for detector resolution, such events must result from an accidental overlap. The LPS information from these events was then combined with a sample of non-diffractive DIS Monte Carlo events generated using DJANGOH [33]. The resulting sample was normalized to match the upper tail of the δ^+ distribution for the data shown in Fig. 2. With this method, the level of background contamination, after all selection cuts, was estimated to be 5.2%. Its contribution was statistically subtracted in all results presented below.

Figure 3 shows the distributions of Q^2, W, x_L and $-t$ for events which pass all selection cuts except the ones imposed on the variables shown (indicated by the arrows). Also shown in the figure are the distributions from the modified RAPGAP simulation plus background which was normalized so that the weighted sum of the modified RAPGAP and the background Monte Carlo events describes the Q^2 distribution in the selected range, see Fig. 3 (a). The kinematic distributions of the data, with the exception of the t distribution, are well described by the modified RAPGAP Monte Carlo sample in combination with the background sample.

Figure 4 (a-c) shows some of the properties of the hadronic final state: the distribution of the number of EFOs, the EFO energy in the CMS frame of the $\gamma^*\mathbb{P}$ system and η_{max}, where η_{max} is the pseudorapidity of the most-forward calorimeter cluster of energy greater than 400 MeV. The data are well described by the modified RAPGAP sample in combination with the background sample. Figure 4 (d) shows the average M_X reconstructed using the LPS (Eq. (2)) as a function of the invariant mass calculated using EFOs (Eq. (1)). The correlation seen in the data is well reproduced by the Monte Carlo simulation. The fact that the correlation is approximately linear in the selected mass range confirms that the final state is well contained in the ZEUS detector.

Figure 5 shows the distributions of M_X, $x_{\mathbb{P}}$ and β. After the reweighting procedure, all data distributions are well described by the modified RAPGAP Monte Carlo sample. This reweighting, which mainly affected the low M_X and high $x_{\mathbb{P}}$ regions, had little effect on the β distribution which, although peaking at low values, is well described by the relatively flat Pomeron PDFs used in RAPGAP. RIDI (not shown in Figs. 2 to 5) also reproduces the data satisfactorily.

7 Systematic uncertainties

The systematic uncertainties were obtained by studying the sensitivity of the results to the uncertainties in the understanding of the ZEUS detector response and by modifying the analysis procedures as listed below.

Uncertainties related to the understanding of the ZEUS main detector include:

- the uncertainty on the absolute energy scales in each major section of the calorimeter (FCAL, BCAL, and RCAL), which for this analysis was understood to a level of 3% for hadrons and 2% for the scattered positron;

- the uncertainty on the survey measurements of the positions of the major sections of the calorimeter with respect to each other and to the HERA beamline, which are accurate to 1–2 mm.

Uncertainties related to the LPS include:

- possible shifts in x_L, p_X, and p_Y of ± 0.003, ± 10 MeV, and ± 50 MeV, respectively, as determined from an analysis of elastic ρ photoproduction ($ep \to e\rho p$);

- the uncertainty on the beampipe position, as determined by alignment studies, was taken into account by changing the cut on the distance of closest approach of the proton track to the beampipe by ± 400 μm;

- the uncertainty in the Monte Carlo simulation of the proton track reconstruction was taken into account by applying tighter cuts on the quality of the Monte Carlo track.

To check for the effect of possible particle losses into the forward beampipe, and to account for the differences in modeling this forward region in the Monte Carlo generators, the energy deposited in the inner ring of the FCAL, which covers approximately the pseudorapidity range of $2.7 < \eta < 3.9$, was scaled by $\pm 25\%$, as suggested by MC studies.

The normalization of the background from an accidental overlap of a DIS event with an unrelated proton was estimated using the δ^+ distribution of Fig. 2. The uncertainty caused by the background subtraction was determined by changing the background normalization by $\pm 50\%$.

To estimate the model dependence of the results, the data were also corrected using RIDI. The difference between the RIDI and modified RAPGAP results was taken as an estimate of the model uncertainty. This uncertainty was assumed to be symmetric with respect to the nominal results obtained using the modified RAPGAP sample.

The largest contributions to the systematic uncertainty typically originate from the model dependence and the uncertainty in the x_L reconstruction. All systematic uncertainties were assumed to be independent and were calculated separately for positive and negative variations with respect to the nominal value. The total positive and negative systematic uncertainties were calculated as the corresponding sums in quadrature.

8 Global event-shape variables

The results presented here are corrected to the hadron level in the kinematic range defined in Section 4 with at least four stable particles in the final state. A particle is considered stable if its lifetime is longer than 3×10^{-10} s. If the lifetime is shorter than 3×10^{-10} s, the daughter particles (with lifetime $> 3 \times 10^{-10}$ s) are included. This corresponds to the final-state definition used by e^+e^- experiments [8].

8.1 Thrust and sphericity

The event-shape-variable thrust (T) is calculated by determining the unit vector $\hat{\boldsymbol{n}}$ which maximizes

$$T(\hat{\boldsymbol{n}}) = \frac{\sum_i |\hat{\boldsymbol{n}} \cdot \boldsymbol{p}_i|}{\sum_i |\boldsymbol{p}_i|},$$

where $\boldsymbol{p}_i$ is the three-momentum of a final-state particle and the sum is over all particles belonging to the system under study. The resulting axis $\hat{\boldsymbol{n}}$ is called the thrust axis and $T(\hat{\boldsymbol{n}})$ is the thrust value. For collimated two-jet events, the value of T approaches 1, while events with an isotropic shape yield values close to 0.5.

The sphericity (S) is defined as

$$S = \frac{3}{2}(\lambda_2 + \lambda_3),$$

where λ_2 and λ_3 are the two smallest eigenvalues (corresponding to orthogonal eigenvectors) of the sphericity tensor

$$S^{\alpha\beta} = \frac{\sum_i p_i^\alpha p_i^\beta}{\sum_i |\boldsymbol{p}_i|^2} \quad \alpha, \beta = x, y, z. \tag{3}$$

For isotropic events, S approaches 1, and for collimated two-jet events, S is close to 0.

The sphericity and thrust distributions in the CMS of the final state in diffractive DIS are shown in Fig. 6 for two bins of M_X, and are compared to the ones observed in e^+e^- annihilation from the TASSO collaboration [8] at $\sqrt{s} = \langle M_X \rangle$. The diffractive events show thrust (sphericity) distributions which are broader and shifted to lower (higher) values compared to the e^+e^- results, indicating that they are more isotropic. The diffractive events become more collimated as M_X increases, a trend also observed in e^+e^- annihilation. If the virtual photon in diffractive DIS fluctuates only into a $q\bar{q}$ state, the resulting hadronic final state should develop in a manner similar to $e^+e^- \to q\bar{q}$ at a CMS energy $\sqrt{s} = \langle M_X \rangle$. Deviations from this e^+e^--type of behavior are expected, however, since

there is a significant contribution from the $q\bar{q}g$ diagram in the color field of the proton (Fig. 1(d)), which is not present in e^+e^- collisions, where gluons can only be produced via higher-order QCD radiation.

Figures 7 (a) and (c) show the average values of thrust, $\langle T \rangle$, and sphericity, $\langle S \rangle$, measured in six bins of M_X. The value of $\langle T \rangle$ increases and $\langle S \rangle$ decreases with increasing M_X with slopes similar to those found in the e^+e^- data [8]. On average, the diffractive events are less collimated than e^+e^- events at a similar CMS energy.

Figures 7 (b) and (d) show the same data, but now compared to several Monte Carlo models[2]. Also plotted in Fig. 7 (b) are the average thrust values measured by the H1 collaboration using a diffractive DIS sample tagged with rapidity gaps [11]. The present measurements are in good agreement with the H1 results which have been corrected to the full phase space by a MC simulation. The results are also consistent with those presented in a previous ZEUS publication [10], which were obtained for a small range in η.

The Monte Carlo models of diffractive scattering reproduce the general trend of the data. RAPGAP and SATRAP-CDM give a good description of $\langle T \rangle$ over almost the full M_X range, while RIDI fails for $M_X \leq 20$ GeV. The diffractive models produce events more isotropic than the ones generated with JETSET and measured in e^+e^- annihilation. This is mainly due to the inclusion of $q\bar{q}g$ final states. Figures 7 (b) and (d) also show the RAPGAP contribution for the $q\bar{q}$ diagram alone. These curves demonstrate the need for the $q\bar{q}g$ contribution, especially at the higher M_X values.

The final state measured in terms of thrust and sphericity has no strong dependence on any kinematic variable other than M_X. Figure 8 shows $\langle T \rangle$ as a function of M_X for $x_{I\!P} < 0.01$, where Pomeron exchange dominates, and for $x_{I\!P} > 0.01$, where Reggeon exchange may become more important. No significant differences are observed and all models give a reasonable description of the data. The data were also split into two samples of Q^2, t and x; the dependence on these variables was less pronounced than that for $x_{I\!P}$.

8.2 Transverse momenta in and out of the event plane

The shape of the system X was also studied in terms of two more variables, $P^2_{T,in}$ and $P^2_{T,out}$, which measure the transverse momentum *in* and *out* of the event plane. The event plane is defined by the eigenvectors of the sphericity tensor associated with the two largest eigenvalues, λ_1 and λ_2 (see Eq. (3)). These transverse momenta have also been studied in e^+e^- experiments, since they are sensitive to gluon bremsstrahlung. They are evaluated

[2] Henceforth, all comparisons of the data are made to MC models that have not been reweighted in the manner described in Sec. 6.

by multiplying the average momentum squared of the n particles in the event by the two smallest sphericity eigenvalues λ_2 and λ_3, respectively:

$$P^2_{T,in} = \frac{\sum_i p_i^2}{n}\lambda_2, \quad (4)$$

$$P^2_{T,out} = \frac{\sum_i p_i^2}{n}\lambda_3, \quad (5)$$

where p_i^2 is the squared momentum of the ith particle in the event. By definition, $P^2_{T,in} > P^2_{T,out}$. The observation of a difference in the M_X behavior of these two variables could be explained by the presence of events of planar shape, such as events with three partons in the final state.

Figures 9 (a) and (b) show the average values of $P^2_{T,in}$ and $P^2_{T,out}$ for the diffractive DIS sample as a function of M_X. On average, $P^2_{T,in}$ is about a factor of three larger than $P^2_{T,out}$. The dependence of $P^2_{T,in}$ on M_X is almost linear over the range studied, while the M_X dependence of $P^2_{T,out}$ becomes weaker as M_X increases, indicating that the diffractive events become more planar. Figure 9 also shows the predictions of the diffractive DIS generators and JETSET. The RAPGAP and SATRAP-CDM samples give a good description of $P^2_{T,in}$ for low masses, but underestimate its value for $M_X \gtrsim 15$ GeV. RIDI overestimates $P^2_{T,in}$ for most of the measured M_X region. Transverse momentum out of the event plane can be produced by the fragmentation process. While RAPGAP and SATRAP-CDM give a reasonable description of the data, RIDI slightly overestimates the data at low M_X values. The transverse momentum distributions in and out of the event plane predicted by JETSET are in excellent agreement with the diffractive scattering data.

In summary, the diffractive hadronic final state shows trends in $\langle T \rangle$ and $\langle S \rangle$ different from those observed in e^+e^- annihilation. These differences can be explained by the presence of $q\bar{q}g$ events from BGF (RAPGAP) or from photon dissociation (SATRAP-CDM, RIDI) which are absent in e^+e^- annihilation and JETSET, where the only source of gluons in the final state is from QCD radiation. The transverse momentum out of the event plane obtained from diffractive Monte Carlo models and JETSET reproduces the data, indicating that the hadronization process is consistently modeled and is similar in diffractive DIS and e^+e^- annihilation.

9 Thrust axis orientation

The orientation of the entire hadronic final state, X, with respect to the $\gamma^*\mathbb{P}$ axis can be studied by measuring the angle θ_{Thrust} (as shown in Fig. 1 (b)) between this axis and the thrust axis.

The values of $\theta_{\rm Thrust}$ and the transverse momentum, $P_{\rm T}^{\rm Thrust}$, relative to the thrust axis, defined by

$$P_{\rm T}^{\rm Thrust} = \frac{M_X}{2} \sin\theta_{\rm Thrust}, \tag{6}$$

are sensitive to various sources of transverse momentum. These include the intrinsic transverse momentum, k_T, of the partons in the proton, which was found to be $1.69 \pm 0.18^{+0.18}_{-0.20}$ GeV in a recent ZEUS publication [34], intrinsic transverse momentum of the partons in the Pomeron, and contributions of hard processes, e.g. final-state gluon emission [35].

Figure 10 (a) shows the average thrust angle $\langle\theta_{\rm Thrust}\rangle$ as a function of M_X. The angle is largest at small masses and falls off steeply as M_X increases, indicating that the event becomes more aligned with the $\gamma^*\mathbb{P}$ axis as the CMS energy increases. This general trend is described by all Monte Carlo models shown, but only RIDI produces a thrust angle as large as that observed in the data. SATRAP-CDM and RAPGAP fall about equally short of the observed angles. Given that the hadronization is well described by all Monte Carlo models (see Section 8.2), the measurement of $\langle\theta_{\rm Thrust}\rangle$ implies that additional sources of transverse momentum as discussed above must be important. Indeed, the approach implemented in RIDI favors the production of partons with relatively large transverse momenta, typically of the order of 1 GeV [24].

Figure 10 (b) shows that the average transverse momentum, $\langle p_{\rm T}^{\rm Thrust}\rangle$, produced in diffractive scattering is almost independent of M_X for $M_X > 10$ GeV, with an average value of about 2 GeV. In this region of M_X, the independence is correctly reproduced by all Monte Carlo models, but the RAPGAP prediction is too low. The need for the $q\bar{q}g$ contribution is illustrated by the curve showing only that part of the RAPGAP prediction corresponding to the $q\bar{q}$ final state.

10 Energy flow

Another measurement of the event topology is the distribution of energy as a function of the pseudorapidity of a hadron with respect to the $\gamma^*\mathbb{P}$ CMS axis. This distribution, commonly referred to as the energy flow, is shown in Fig. 11 for data in three M_X ranges. The data for low M_X have a Gaussian-like shape, but for $M_X > 7.5$ GeV a structure with two peaks develops. This structure becomes more pronounced as the mass increases. A slight asymmetry develops in the data, with more energy being produced in the γ^* hemisphere. For comparison, the predictions from the RAPGAP, SATRAP-CDM and RIDI Monte Carlo generators are also shown. The SATRAP-CDM and RAPGAP generators predict too broad a rapidity distribution, and display a separation between the γ^* and

$\mathbb{P}$ hemispheres in the lowest M_X bin that is not exhibited by the data. RIDI gives a reasonable description of the data in the lowest M_X bin but has a different shape at higher M_X. The asymmetry indicated in the data is slightly larger than that produced by the diffractive Monte Carlo models. For those values of $|\eta|$ at which the H1 collaboration has also published data [5], the energy flow is in good agreement, except at the highest M_X where the H1 data are somewhat narrower.

Figure 12 shows the distribution of transverse energy, $E_T = \sum E_i \sin\theta_i$, as a function of η. Similar discrepancies between the data and the Monte Carlo events were observed for the transverse-energy flow as was observed for the energy-flow distribution.

11 Seagull distribution

The small asymmetry between positive and negative η observed in the energy-flow plot of Fig. 11 can be further investigated using the distribution of transverse momentum of the particles belonging to the system X.

In inclusive DIS, $ep \to eX$, the fragmentation of the hadronic system occurs between the struck quark (forming the system X) and the remaining quarks in the proton (forming the proton remnant). Measurements in the Breit frame [36] have shown that, whereas the particle multiplicity and momentum distributions in the hemisphere of the struck quark are roughly consistent with those measured in $e^+e^- \to q\bar{q}$, particles are produced with smaller average transverse momentum in the proton-remnant hemisphere.

In diffractive DIS, an asymmetry in the momentum distribution between the γ^* and $\mathbb{P}$ hemispheres could be observed if the Pomeron behaves as an extended object like the proton and produces a remnant after the scattering process. This asymmetry is usually investigated by studying single-particle distributions as a function of the scaled longitudinal momentum, x_F, and the momentum transverse to the photon direction, p_T. The photon direction defines the longitudinal axis in the $\gamma^*\mathbb{P}$ CMS as well as in the γ^*p CMS. If p_T and p_L are the momentum components of a final-state hadron perpendicular and parallel, respectively, to this axis, the variable x_F is given by:

$$x_F = p_L / p_L^{max},$$

where positive x_F is in the direction of the γ^* and p_L^{max} is the maximum kinematically allowed value of p_L. In the $\gamma^*\mathbb{P}$ CMS, $p_L^{max} = M_X/2$. For the γ^*p case, $p_L^{max} = W/2$.

The average p_T^2 of particles as a function of x_F, commonly referred to as the "seagull plot", is shown in Fig. 13 for $11 < M_X < 17.8$ GeV. Also plotted are γ^*p data from the EMC [37] collaboration at $W = 14$ GeV, equal to the average value of M_X in this bin.

The EMC DIS $\mu p \to \mu X$ data indicate a suppression of the average p_T^2 associated with a proton remnant which is not as apparent in the diffractive data in this mass range.

Shown in Fig. 14 (a)-(c) is the seagull plot for three different M_X bins compared with the predictions from RAPGAP, SATRAP-CDM and RIDI. The data exhibit a growing asymmetry as M_X increases. This asymmetry can also be seen in the ratios of the average squared transverse-momentum in the γ^* and $\mathbb{P}$ hemispheres as a function of $|x_F|$ (Fig. 14 (d)-(f)). The data are well reproduced by both RAPGAP and RIDI, while for $M_X > 16$ GeV, the transverse momentum generated by SATRAP-CDM is smaller than in the data. RAPGAP and SATRAP-CDM describe the size of the asymmetry correctly in all M_X bins, while for $M_X > 16$ GeV RIDI slightly underestimates the transverse momentum in the $\mathbb{P}$ direction, resulting in a slightly larger asymmetry than that seen in the data. RAPGAP produces this asymmetry by including a Pomeron remnant. RIDI and SATRAP-CDM, in contrast, produce the asymmetry via the $q\bar{q}g$ diagram.

12 Conclusion

A study of the hadronic system, X, in the reaction $ep \to eXp$ has been reported for the kinematic range $4 < M_X < 35$ GeV, $4 < Q^2 < 150$ GeV^2, $0.0003 < x_{\mathbb{P}} < 0.03$ and $70 < W < 250$ GeV. The use of the LPS allows diffractive events to be tagged without applying cuts on the system X. It also provides a powerful constraint on the diffractive kinematics, allowing, for example, an accurate determination of the $\gamma^*\mathbb{P}$ axis in the center-of-mass frame of the system X.

The diffractive hadronic final state becomes more collimated as the invariant mass M_X of the system increases. This trend is similar to the one observed in e^+e^- annihilation. However, on average the diffractive final state is more isotropic. This can be attributed to contributions not present in e^+e^- annihilation, such as the boson-gluon fusion process in the resolved Pomeron approach, or $q\bar{q}g$ production from the dissociation of the virtual photon.

The mean transverse momentum out of the event plane is similar to that found in e^+e^- annihilation, indicating the universality of the hadronization. Even after considering the broadening effects of hadronization, it is apparent that more k_T than is usually associated with the resolved Pomeron Monte Carlo approach is required to accommodate the large thrust angle and narrow energy flows at low M_X.

Particle production becomes asymmetric along the $\gamma^*\mathbb{P}$ axis as M_X increases, resulting in more average transverse momentum in the virtual-photon hemisphere. This asymmetry is consistent with both the concept of a remnant in the resolved Pomeron model and with the production of $q\bar{q}g$ final states in the photon-dissociation approach. The comparison

with the Monte Carlo models suggests that a dominant gluon contribution to the partonic final state is necessary.

The invariant mass, M_X, of the hadronic system is the only variable upon which the characteristics of the system was found to depend. The system is independent of the momentum transfer at either the positron vertex, Q^2, or at the proton vertex, t. Neither is there any dependence on x or on the fractional momentum of the Pomeron, $x_{I\!P}$.

Many models of diffraction are able to reproduce the measured diffractive cross sections. However, none of the models discussed here is able to describe all aspects of the data. It is clear, therefore, that measurements of the detailed characteristics of diffractive events, such as presented in this paper, will become more and more crucial in understanding the underlying physics of diffraction in deep inelastic scattering.

Acknowledgments

This measurement was made possible by the inventiveness and the diligent efforts of the HERA machine group. The strong support and encouragement of the DESY directorate has been invaluable. The design, construction, and installation of the ZEUS detector has been made possible by the ingenuity and dedicated effort of many people from inside DESY and from the home institutes who are not listed as authors. Their contributions are acknowledged with great appreciation. We acknowledge support by the following: the Natural Sciences and Engineering Research Council of Canada (NSERC); the German Federal Ministry for Education and Science, Research and Technology (BMBF), under contract numbers 057BN19P, 057FR19P, 057HH19P, 057HH29P, 057SI75I; the MINERVA Gesellschaft für Forschung GmbH, the Israel Science Foundation, the U.S.-Israel Binational Science Foundation, the Israel Ministry of Science and the Benozyio Center for High Energy Physics; the German-Israeli Foundation, the Israel Science Foundation, and the Israel Ministry of Science; the Italian National Institute for Nuclear Physics (INFN); the Japanese Ministry of Education, Science and Culture (the Monbusho) and its grants for Scientific Research; the Korean Ministry of Education and Korea Science and Engineering Foundation; the Netherlands Foundation for Research on Matter (FOM); the Polish State Committee for Scientific Research, grant no. 2P03B04616, 620/E-77/SPUB-M/DESY/P-03/DZ 247/2000 and 112/E-356/SPUB-M/DESY/P-03/DZ 3001/2000, and by the German Federal Ministry for Education and Science, Research and Technology (BMBF); the Fund for Fundamental Research of Russian Ministry for Science and Education and by the German Federal Ministry for Education and Science, Research and Technology (BMBF); the Spanish Ministry of Education and Science through funds provided by CICYT; the Particle Physics and Astronomy Research Council, UK; the US Department of Energy; the US National Science Foundation.

References

[1] ZEUS Collaboration, M. Derrick et al., Phys. Lett. B **315**, 481 (1993);
H1 Collaboration, T. Ahmed et al., Nucl. Phys. **B429,** 477 (1994).

[2] ZEUS Collaboration, J. Breitweg et al., Eur. Phys. J. C **1**, 81 (1998).

[3] H1 Collaboration, C. Adloff et al., Z. Phys. C **76**, 613 (1997).

[4] H1 Collaboration, C. Adloff et al., Eur. Phys. J. C **5**, 439 (1998).

[5] H1 Collaboration, C. Adloff et al., Phys. Lett. B **428**, 206 (1998).

[6] ZEUS Collaboration, J. Breitweg et al., Eur. Phys. J. C **1**, 81 (1998);
ZEUS Collaboration, J. Breitweg et al., Eur. Phys. J. C **6**, 43 (1999).

[7] See e.g. *Proceedings of the Workshop on Future Physics at HERA*, Volume 2, G. Ingelman, A. De Roeck, and R. Klanner (eds.), DESY (1996), and references therein.

[8] PLUTO Collaboration, C. Berger et al., Z. Phys. C **12**, 297 (1982);
MARK II Collaboration, A. Peterson et al., Phys. Rev. D **37**, 1 (1988);
TASSO Collaboration, W. Braunschweig et al., Z. Phys. C **47**, 187 (1990).

[9] ZEUS Collaboration, M. Derrick et al., Z. Phys. C **73**, 253 (1997).

[10] ZEUS Collaboration, J. Breitweg et al., Phys. Lett. B **421**, 368 (1998).

[11] H1 Collaboration, C. Adloff et al., Eur. Phys. J. C **1**, 495 (1998).

[12] J. Ellis, G. G. Ross and J. Williams, Eur. Phys. J. C **10**, 443 (1999).

[13] MARK-J Collaboration, D.P. Barber et al., Phys. Rev. Lett. **43**, 830 (1979);
TASSO Collaboration, R. Brandelik et al., Phys. Lett. B **86**, 243 (1979);
PLUTO Collaboration, C. Berger et al., Phys. Lett. B **86**, 418 (1979);
JADE Collaboration, W. Bartel et al., Phys. Lett. B **91**, 142 (1980);
P. Söding and G. Wolf, Ann. Rev. Nucl. Part. Sci. **31**, (1981).

[14] ZEUS Collaboration, U. Holm (ed.), The ZEUS Detector, Status Report 1993, DESY (1993) (unpublished), `http://www-zeus.desy.de/bluebook/bluebook.html`.

[15] N. Harnew et al., Nucl. Instrum. Methods Phys. Res. A **279**, 290 (1989);
B. Foster et al., Nucl. Phys. B (Proc. Suppl.) **32**, 181 (1993);
B. Foster et al., Nucl. Instrum. Methods Phys. Res. A **338**, 254 (1994).

[16] M. Derrick et al., Nucl. Instrum. Methods Phys. Res. A **309**, 77 (1991);
A. Andresen et al., Nucl. Instrum. Methods Phys. Res. A **309**, 101 (1991);
A. Caldwell et al., Nucl. Instrum. Methods Phys. Res. A **321**, 356 (1992);
A. Bernstein et al., Nucl. Instrum. Methods Phys. Res. A **336**, 23 (1993).

[17] S. Bentvelsen, J. Engelen and P. Kooijman, *Proceedings of the Workshop on Physics at HERA*, Volume 1, W. Buchmüller and G. Ingelman (eds.) , DESY (1991) p. 23;
K. C. Hoeger, ibid. p. 43.

[18] ZEUS Collaboration, M. Derrick et al., Z. Phys. C **72**, 399 (1996).

[19] F. Jacquet and A. Blondel, *Proceedings of the study of an* ep *facility for Europe*, U. Amaldi (ed.), DESY 79-48, (1979) p. 391.

[20] T. Sjöstrand, Comput. Phys. Commun. **82**, 74 (1994).

[21] G. Ingelman and P. Schlein, Phys. Lett. B **152**, 256 (1985).

[22] RAPGAP version 2.08/06: H. Jung, Comput. Phys. Commun. **86**, 147 (1995).

[23] G. Ingelman, A. Edin and J. Rathsman, Comput. Phys. Commun. **101**, 108 (1997).

[24] RIDI 2.0: M.G. Ryskin and A. Solano, *Proceedings of the Workshop on Monte Carlo Generators for HERA Physics*, G. Grindhammer et al. (eds.), DESY-PROC-1999-02 (1999), p. 386.

[25] M.G. Ryskin, Sov. J. Nucl. Phys. **52**, 529 (1990);
M.G. Ryskin and M. Besancon, *Proceedings of the Workshop on Physics at HERA*, W Buchmüller and G. Ingelman (eds.), (1991), p. 215;
M.G. Ryskin, S.Yu. Sivoklokov and A. Solano, *Proceedings of the 5th Blois Workshop on Elastic and Diffractive Scattering*, H.M. Fried, K. Kang and C-I. Tan (eds.) (1993), p. 181.

[26] CTEQ Collaboration, H.L. Lai et al., Phys. Rev. D *55*, 1280 (1997).

[27] K. Golec-Biernat and M. Wüsthoff, Phys. Rev. D *59*, 014017 (1999);
K. Golec-Biernat and M. Wüsthoff, Phys. Rev. D *60*, 114023 (1999).

[28] H. Kowalski, *Proceedings of the Workshop on New Trends in HERA Physics*, G. Grindhammer, B.A. Kniehl, and G. Kramer (eds.), Ringberg, June 1999, p. 361.

[29] ZEUS Collaboration, S. Chekanov et al., DESY 01-092, submitted to Phys. Lett. B.

[30] T. Yamashita, PhD. Thesis, University of Tokyo (2001), in preparation.

[31] H. Jung and H. Kowalski, private communication.

[32] R. Brun et al., CERN-DD/EE/84-1 (1987).

[33] DJANGO: G.A. Schüler and H. Spiesberger, *Proceedings of the Workshop on Physics at HERA*, Volume 3, W. Buchmüller and G. Ingelman (eds.) , DESY (1991), p. 1419; H. Spiesberger, DJANGOH, `http://www.desy.de/~hspiesb/djangoh.html`.

[34] ZEUS Collaboration, S. Chekanov et al., Phys. Lett. B **511**, 36 (2001).

[35] N.N. Nikolaev, *Proceedings of the workshop on Monte Carlo Generators for HERA Physics*, G. Grindhammer et al. (eds.) DESY-PROC-1999-02 (1999).

[36] H1 Collaboration, S. Aid et al., Z. Phys. C **70**, 609 (1996);
ZEUS Collaboration, J. Breitweg et al., Eur. Phys. J. C **11**, 251 (1999).

[37] EMC Collaboration, M. Arneodo et al., Z. Phys C **35**, 417 (1987).

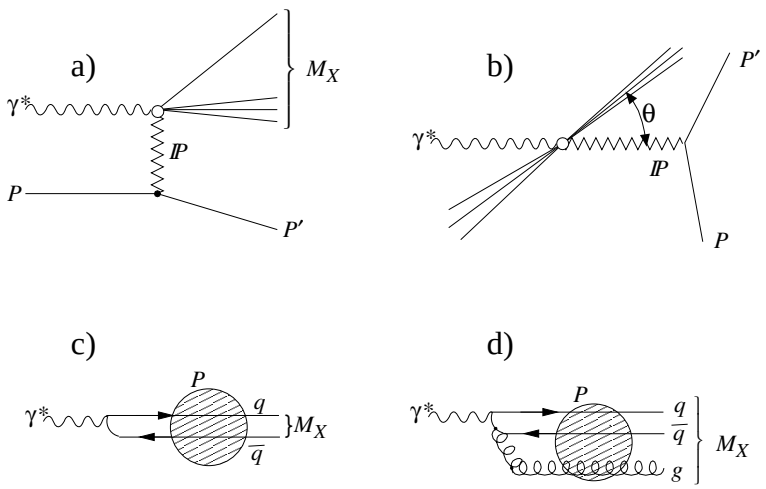

Figure 1: *Different representations of diffractive DIS: (a) basic Pomeron-induced picture of diffraction; (b) the same process, in the $\gamma^*\mathbb{P}$ center-of-mass frame. The thrust angle, $\theta = \theta_{\rm Thrust}$, is defined as the angle between the event axis and the $\gamma^*\mathbb{P}$ axis; (c) diffraction viewed in the rest frame of the proton as the fluctuation of the virtual photon well before the interaction with the proton to a $q\bar{q}$ pair; and (d) into a $q\bar{q}g$ system.*

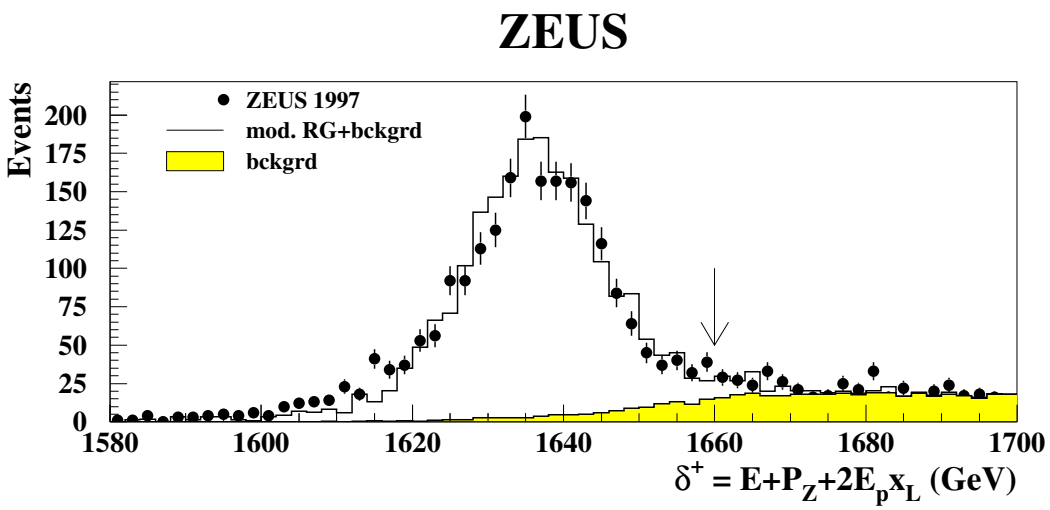

Figure 2: *Normalization of the background. The quantity $\delta^+ = \Sigma(E_i + P_{Zi}) + 2E_p x_L$ is shown for data (points, with statistical error only), background (shaded histogram) and modified RAPGAP plus background (solid histogram). The normalization was obtained as described in the text. The vertical arrow indicates the cut below which events were accepted for the analysis.*

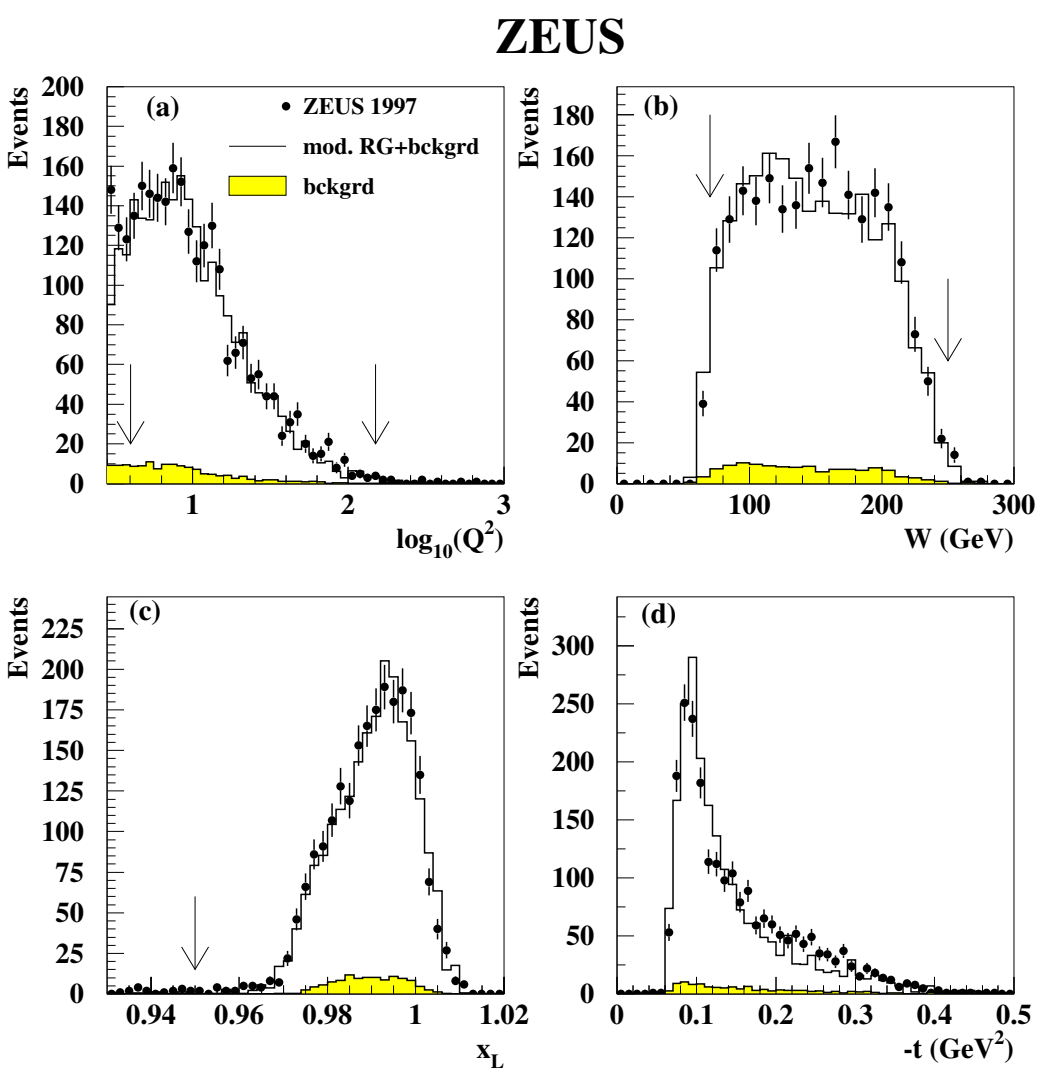

Figure 3: *A comparison of data and Monte Carlo simulation for distributions of the kinematic variables of the diffractive DIS sample: (a) Q^2, (b) W, (c) x_L, and (d) $-t$. The data are displayed as points, with statistical errors only, and are compared to the modified RAPGAP plus background (solid histogram) and background alone (shaded histogram). The normalization was obtained as described in the text. Vertical arrows in (a) and (b) indicate the values of Q^2 and W between which events were selected for this analysis. Events with x_L values below that indicated by the arrow in (c) were rejected. No cut on t was imposed.*

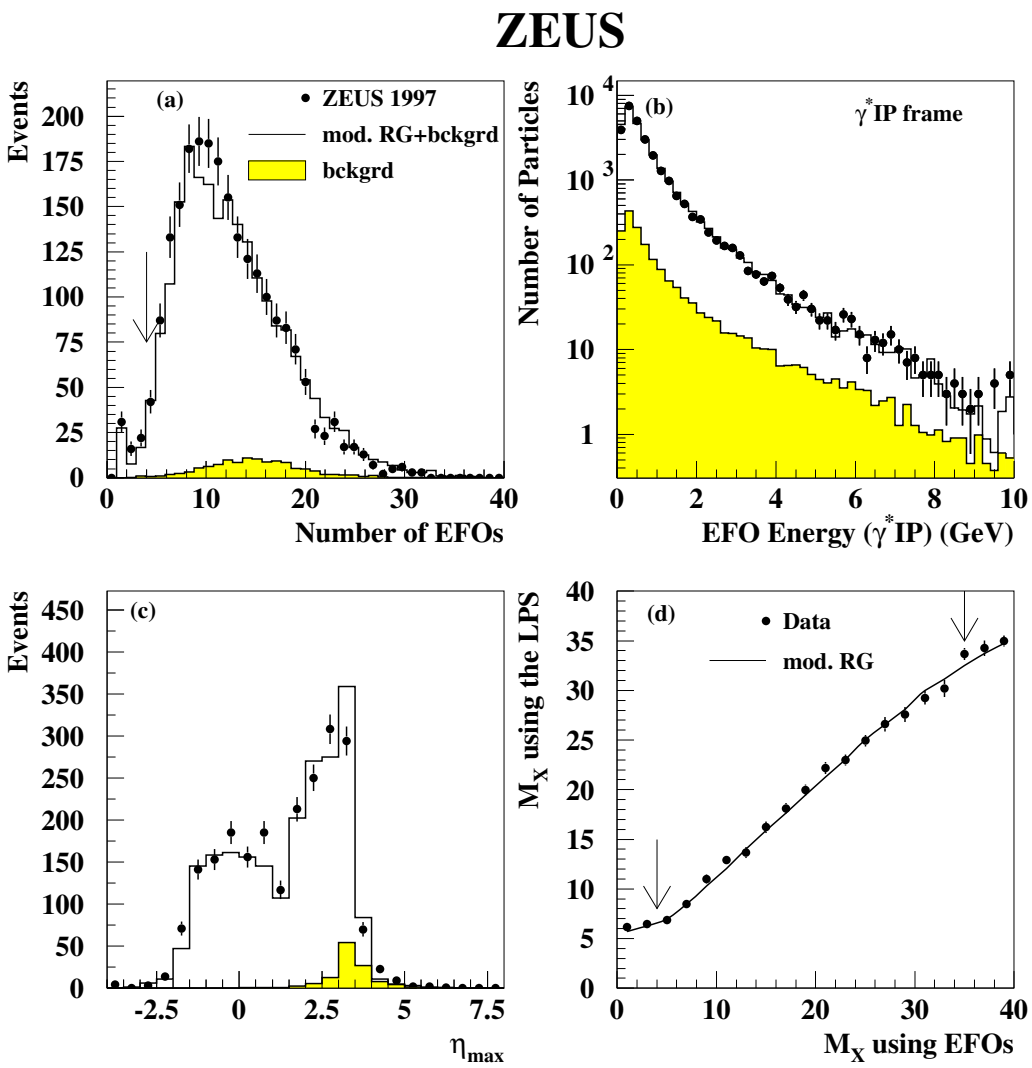

Figure 4: *A comparison of data and Monte Carlo simulation for distributions related to the properties of the reconstructed hadronic final state: (a) the number of EFOs; (b) the energy spectrum of the EFOs in the $\gamma^*\mathbb{P}$ frame; (c) η_{max}; and (d) the average invariant-mass M_X measured with the LPS alone versus M_X determined from the EFOs. The data are displayed as points, with statistical errors only, and are compared to the modified RAPGAP plus background (solid histogram), background alone (shaded histogram) or modified RAPGAP alone (curve in (d)). The vertical arrow in (a) indicates the cut above which events were selected for this analysis. The region of M_X considered is shown by the arrows in (d). No cuts were imposed on the particle energy and η_{max}.*

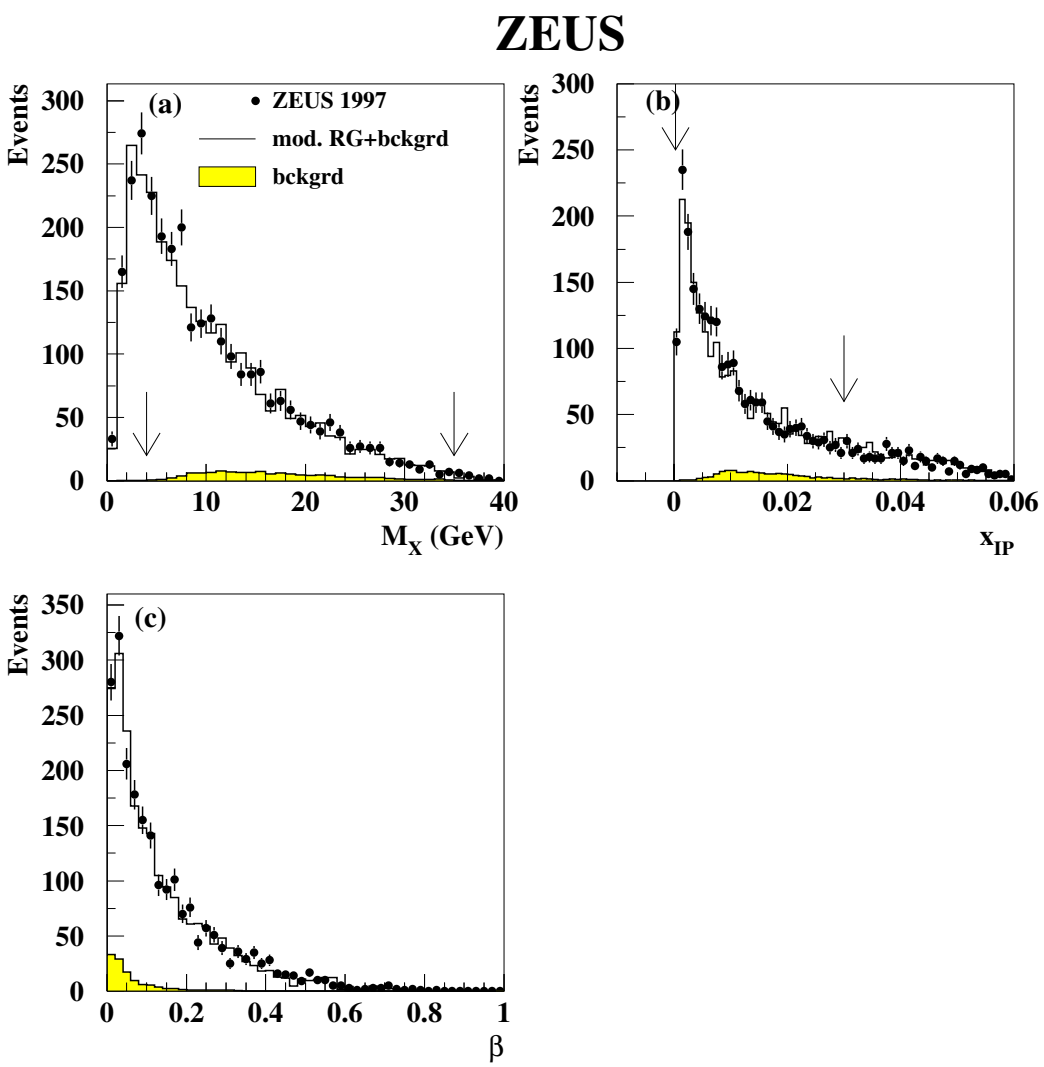

Figure 5: *A comparison of data and Monte Carlo simulation for measured distributions of (a) M_X, (b) $x_{\mathbb{P}}$ and (c) β. The data are displayed as points, with statistical errors only, and are compared to the modified RAPGAP plus background (solid histogram). The background estimate is shown by the shaded histogram. The vertical arrows in (a) and (b) indicate the values of M_X and $x_{\mathbb{P}}$ between which events were selected for this analysis. No cut on β was imposed.*

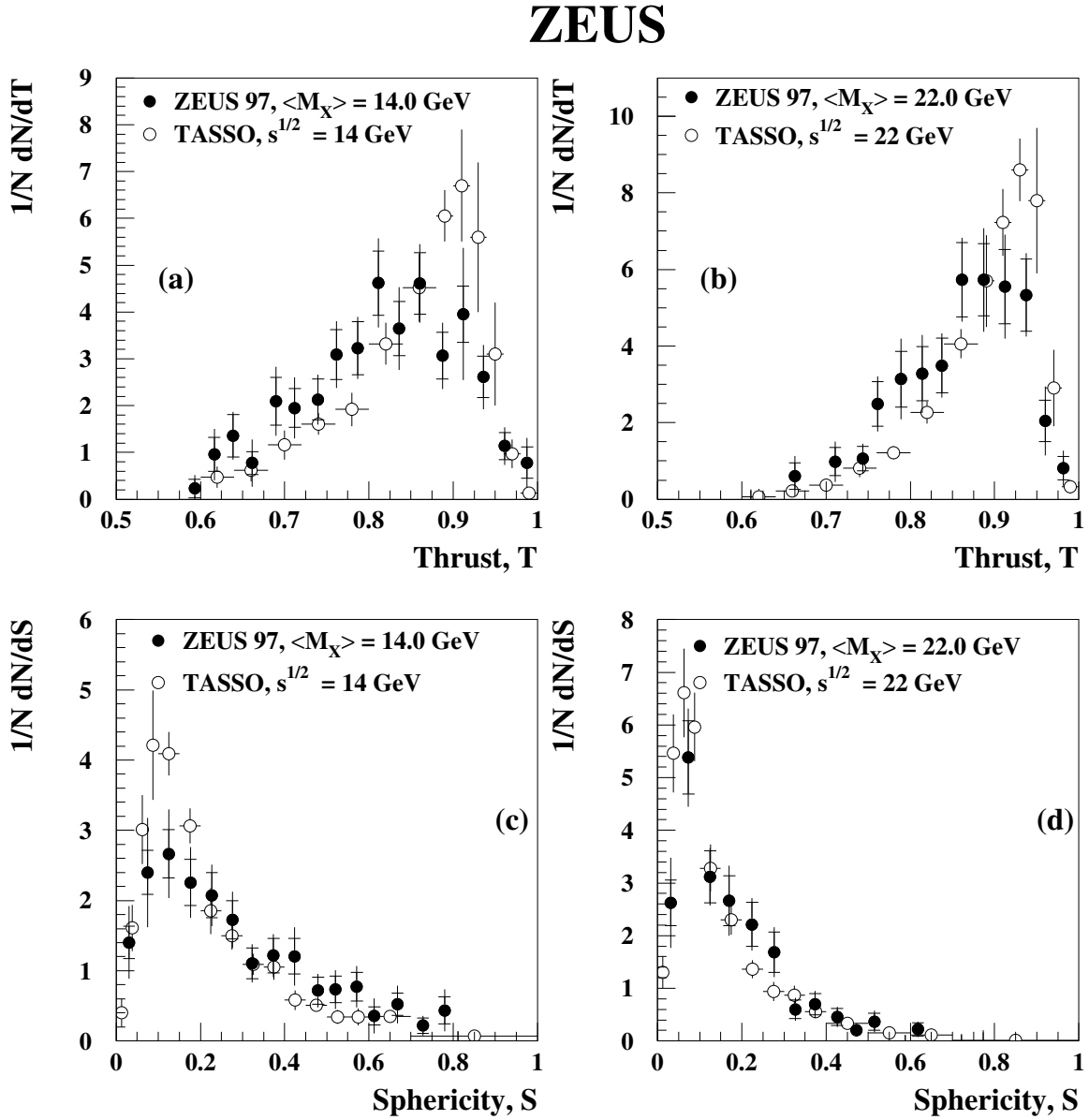

Figure 6: *Thrust, T, and sphericity, S, distributions of the diffractive DIS hadronic final state (filled circles) compared to distributions measured in e^+e^- collisions by the TASSO collaboration [8] (open circles) at the same CMS energies of the system X. In (a) and (c), results for $11 < M_X < 17.8$ GeV ($\langle M_X \rangle = 14.0$ GeV) are compared to measurements in e^+e^- collisions at $\sqrt{s} = 14$ GeV; in (b) and (d), the results for $17.8 < M_X < 27.7$ GeV ($\langle M_X \rangle = 22.0$ GeV) are compared to e^+e^- results at $\sqrt{s} = 22$ GeV. The inner error bars show statistical uncertainties only; the outer bars show the statistical and systematic uncertainties added in quadrature.*

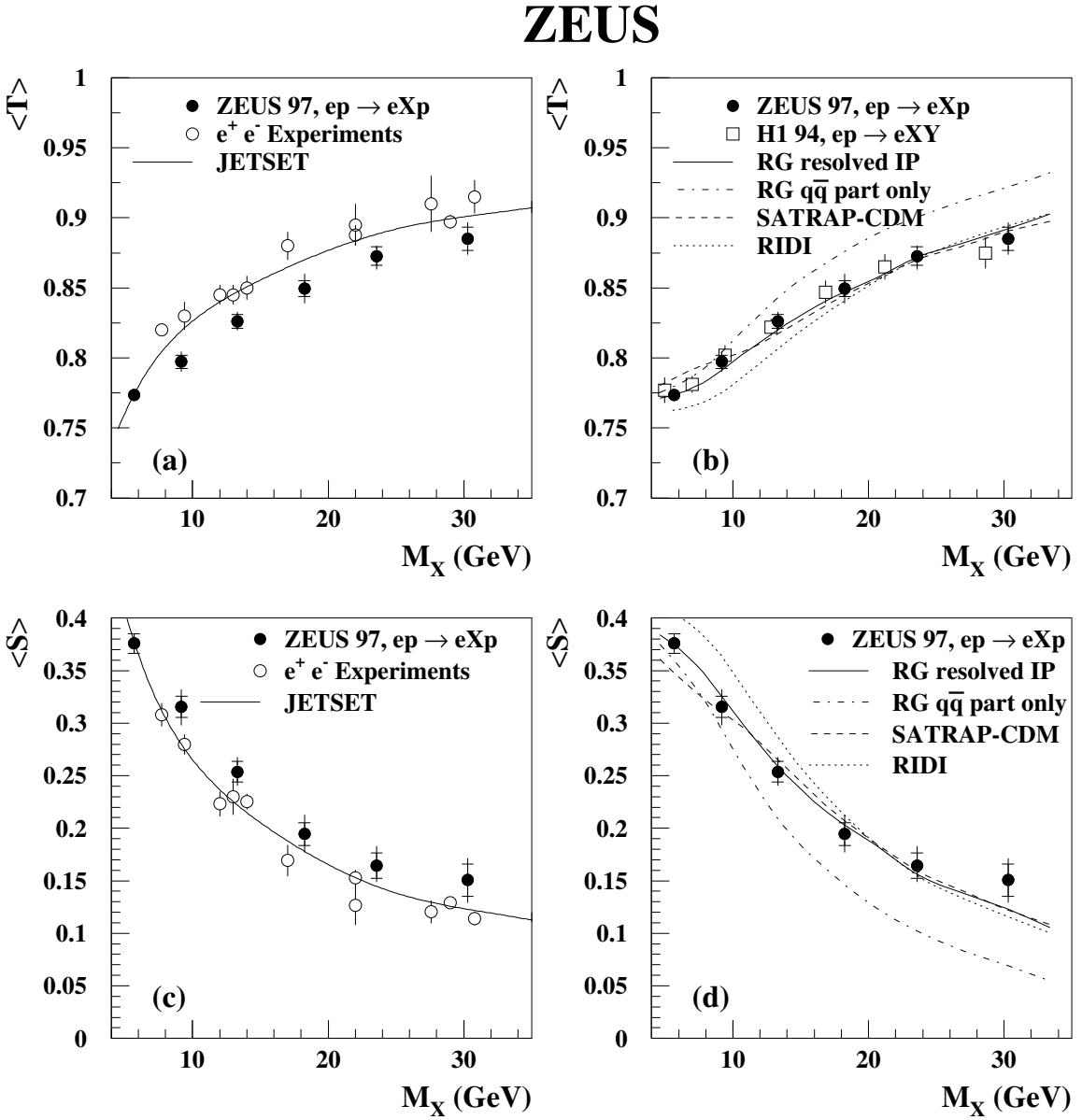

Figure 7: *Average thrust $\langle T \rangle$ and sphericity $\langle S \rangle$ of the diffractive DIS hadronic final state as a function of M_X. Shown for comparison are results from e^+e^- collisions and predictions from three Monte Carlo generators, RAPGAP (solid), RAPGAP $q\bar{q}$ only (dot-dashed), SATRAP-CDM (dashed) and RIDI (dotted). Also shown in (b) are thrust values from the H1 Collaboration for diffractive DIS events tagged using rapidity gaps [11]. The inner error bars show statistical uncertainties only; the outer bars are the statistical and systematic uncertainties added in quadrature.*

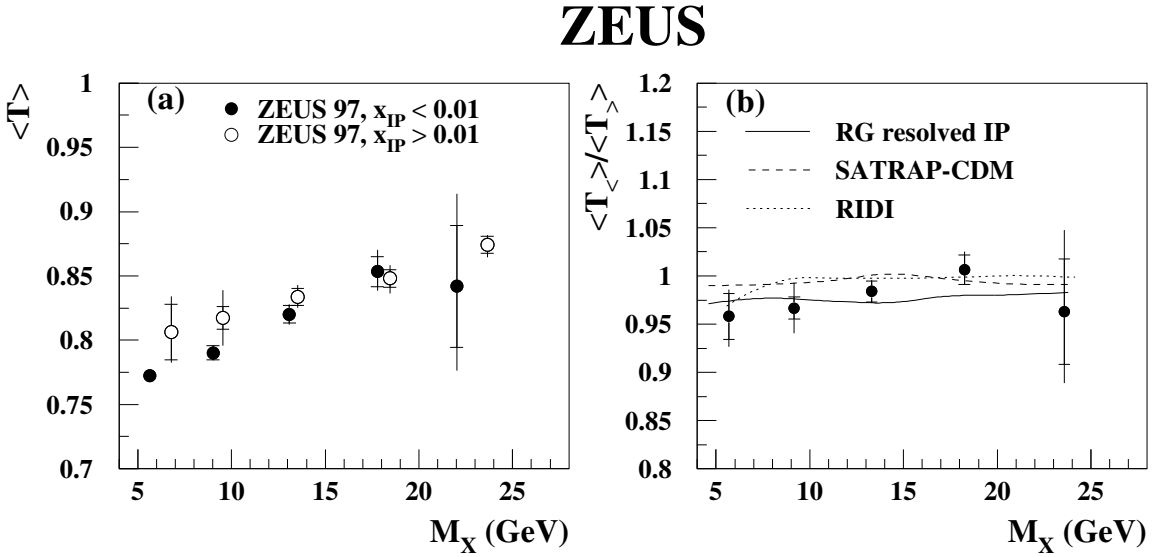

Figure 8: *(a) Average thrust, $\langle T \rangle$, of the diffractive DIS hadronic final state as a function of M_X for two different samples of events: $x_{\mathbb{P}} < 0.01$ (solid circles) and $x_{\mathbb{P}} > 0.01$ (open circles). (b) Ratio of average thrust values $T_< = T(x_{\mathbb{P}} < 0.01)$ and $T_> = T(x_{\mathbb{P}} > 0.01)$ as a function of M_X for data (solid circles), and for predictions from RAPGAP (solid curve), SATRAP-CDM (dashed curve), and RIDI (dotted curve). The inner error bars show statistical uncertainties only; the outer bars are the statistical and systematic uncertainties added in quadrature.*

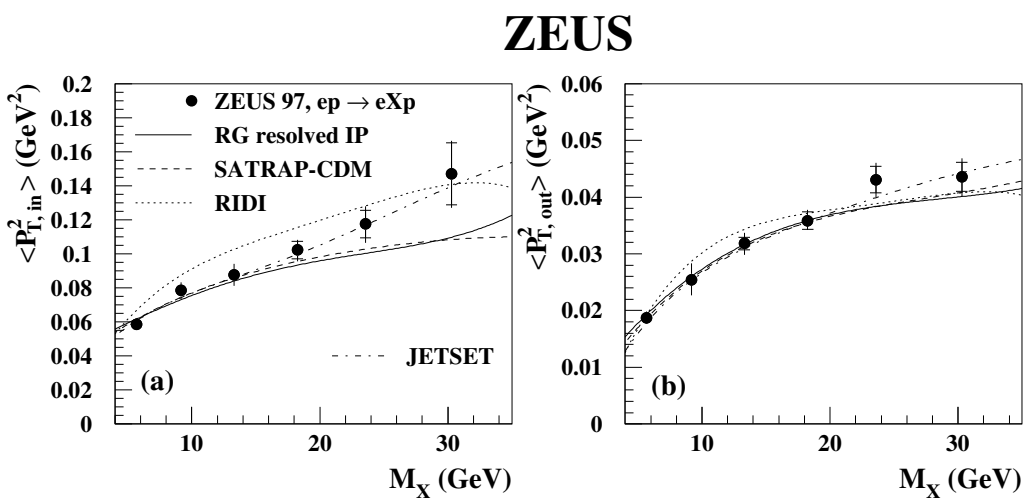

Figure 9: *(a) Average $P^2_{T,in}$ and (b) $P^2_{T,out}$ of the diffractive DIS hadronic final state as a function of M_X. Shown for comparison are predictions from three diffractive Monte Carlo generators, RAPGAP (solid curve), SATRAP-CDM (dashed curve), and RIDI (dotted curve) together with e^+e^- results as simulated by JETSET (dashed-dotted curve). The inner error bars show statistical uncertainties only; the outer bars are the statistical and systematic uncertainties added in quadrature.*

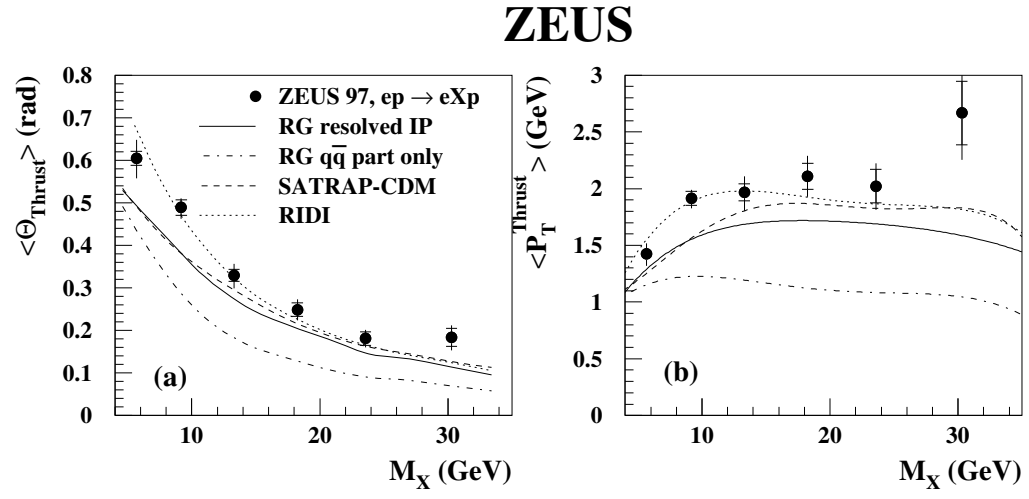

Figure 10: *(a) The average value of the angle θ_{Thrust} of the thrust axis in the $\gamma^*\mathbb{P}$ frame and (b) the corresponding transverse momentum $p_{\mathrm{T}}^{\mathrm{Thrust}}$ compared to the prediction of RAPGAP (solid curve), $q\bar{q}$ part of RAPGAP (dot-dashed), SATRAP-CDM (dashed curve) and RIDI (dotted curve). The inner error bars show statistical uncertainties only; the outer bars show the statistical and systematic uncertainties added in quadrature.*

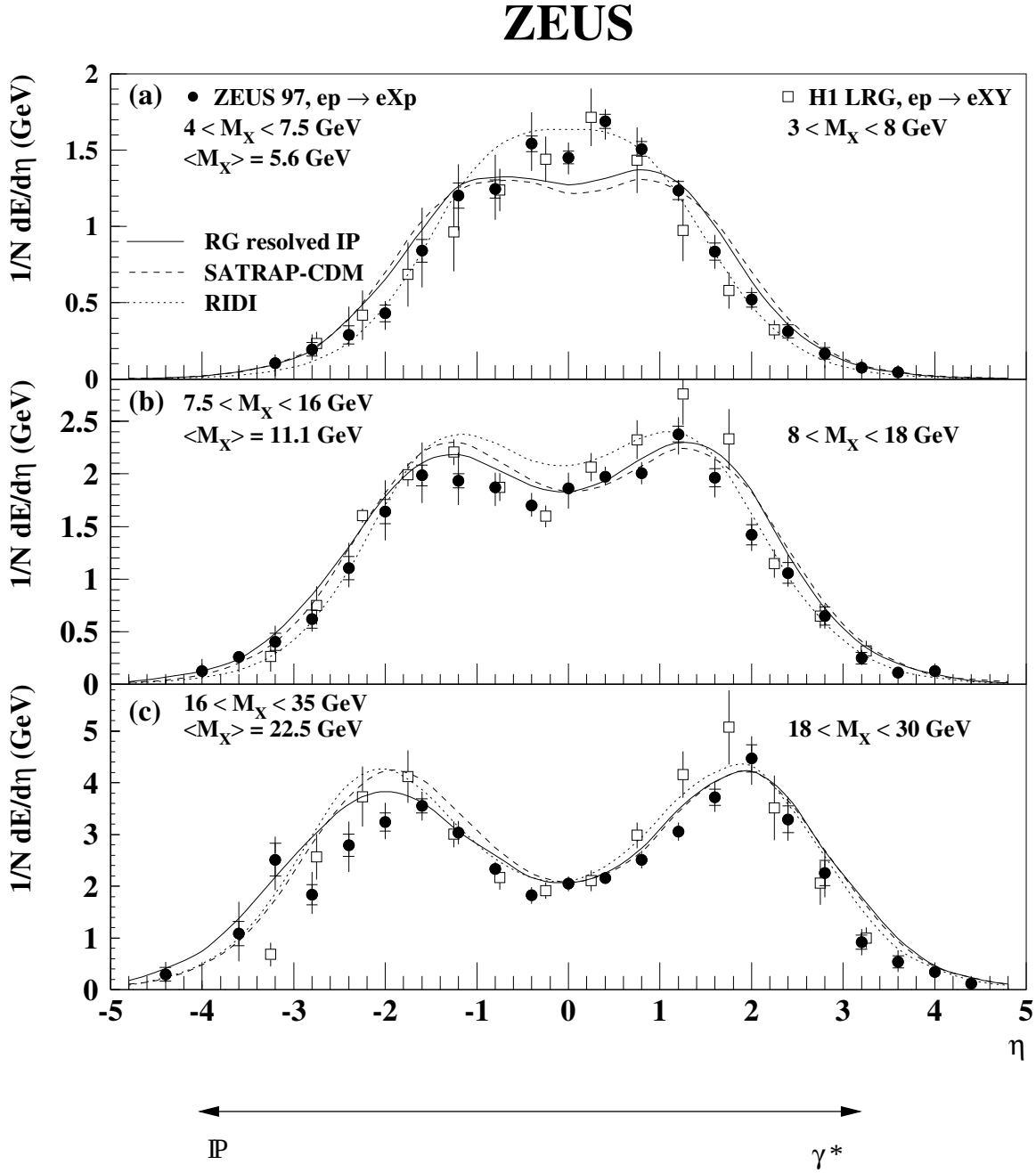

Figure 11: *The energy flow as a function of pseudorapidity, η, in the $\gamma^*\mathbb{P}$-CMS, for various ranges of M_X. The data are shown as solid points, while the Monte Carlo predictions from RAPGAP, SATRAP-CDM and RIDI are shown as solid, dashed and dotted curves, respectively. Positive η is in the direction of the γ^*. The inner error bars show statistical uncertainties only; the outer bars show the statistical and systematic uncertainties added in quadrature. Also shown are the results from the H1 collaboration (open squares) obtained from a measurement based on large rapidity gaps.*

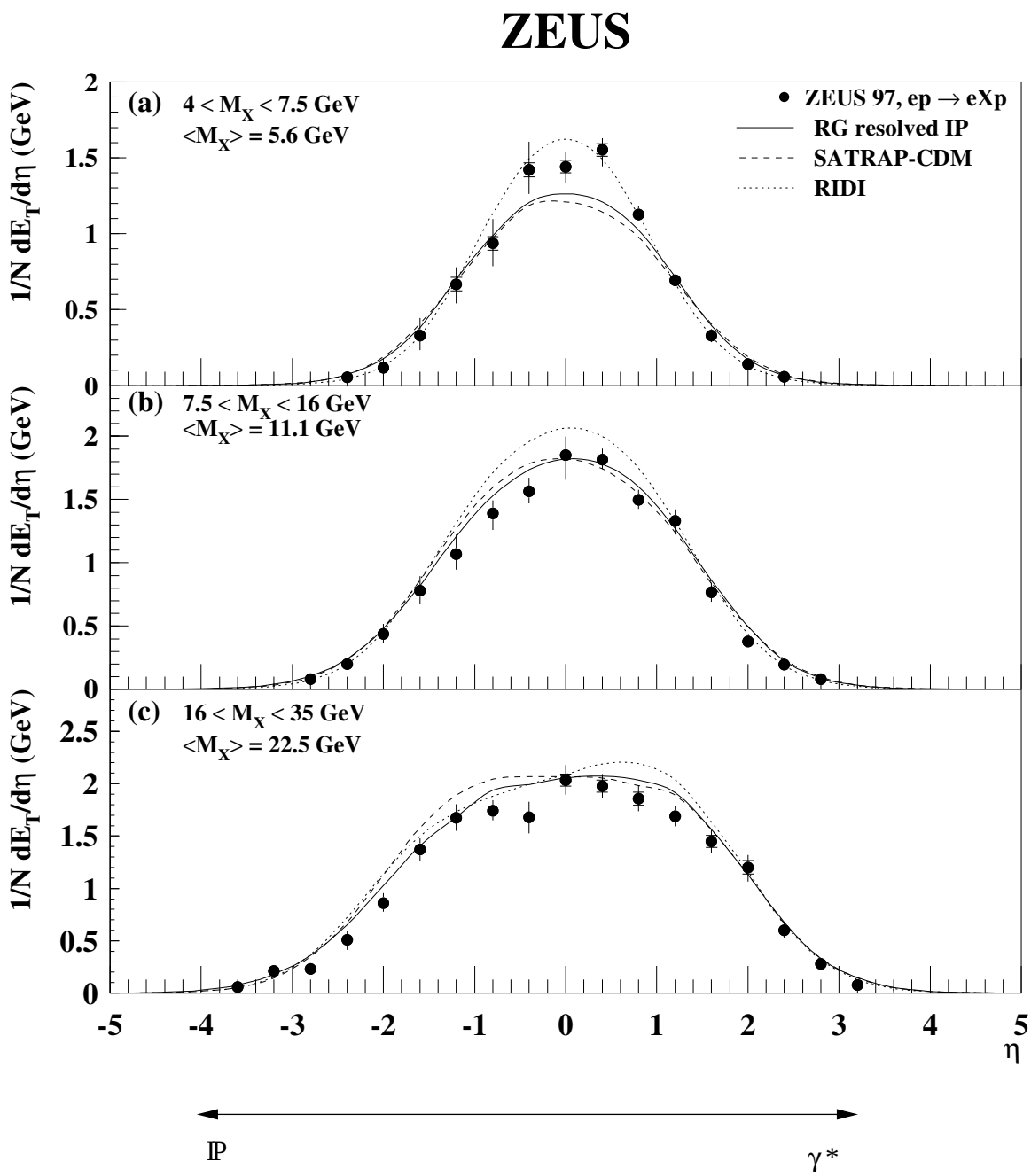

Figure 12: *The transverse energy flow as a function of pseudorapidity, η, in the $\gamma^*\mathbb{P}$-CMS, for various ranges of M_X. The data are shown as solid points, while the Monte Carlo predictions from RAPGAP, SATRAP-CDM and RIDI are shown as solid, dashed and dotted curves, respectively. Positive η is in the direction of the γ^*. The inner error bars show statistical uncertainties only; the outer bars show the statistical and systematic uncertainties added in quadrature.*

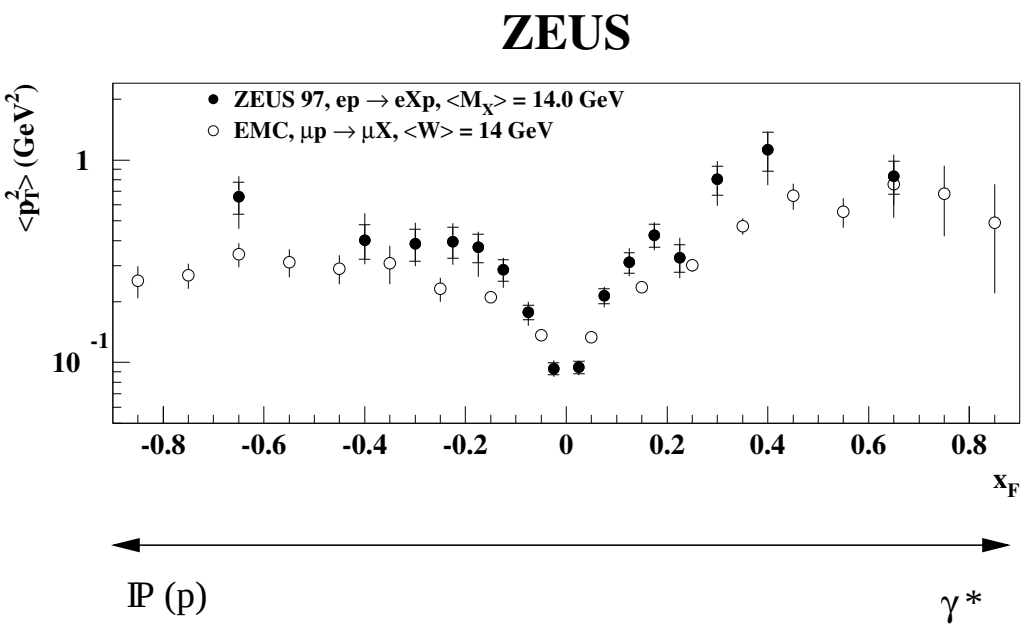

Figure 13: *Average squared transverse momentum of particles measured in the center-of-mass frame of the system X as a function of x_F for diffractive events from this analysis (solid circles) with $11 < M_X < 17.8$ GeV ($\langle M_X \rangle = 14.0$ GeV). Also shown (open circles) is the same quantity for inclusive DIS $\mu p \to \mu X$ data from the EMC collaboration [37] at $W = \langle M_X \rangle$. Positive x_F is in the direction of the virtual photon.*

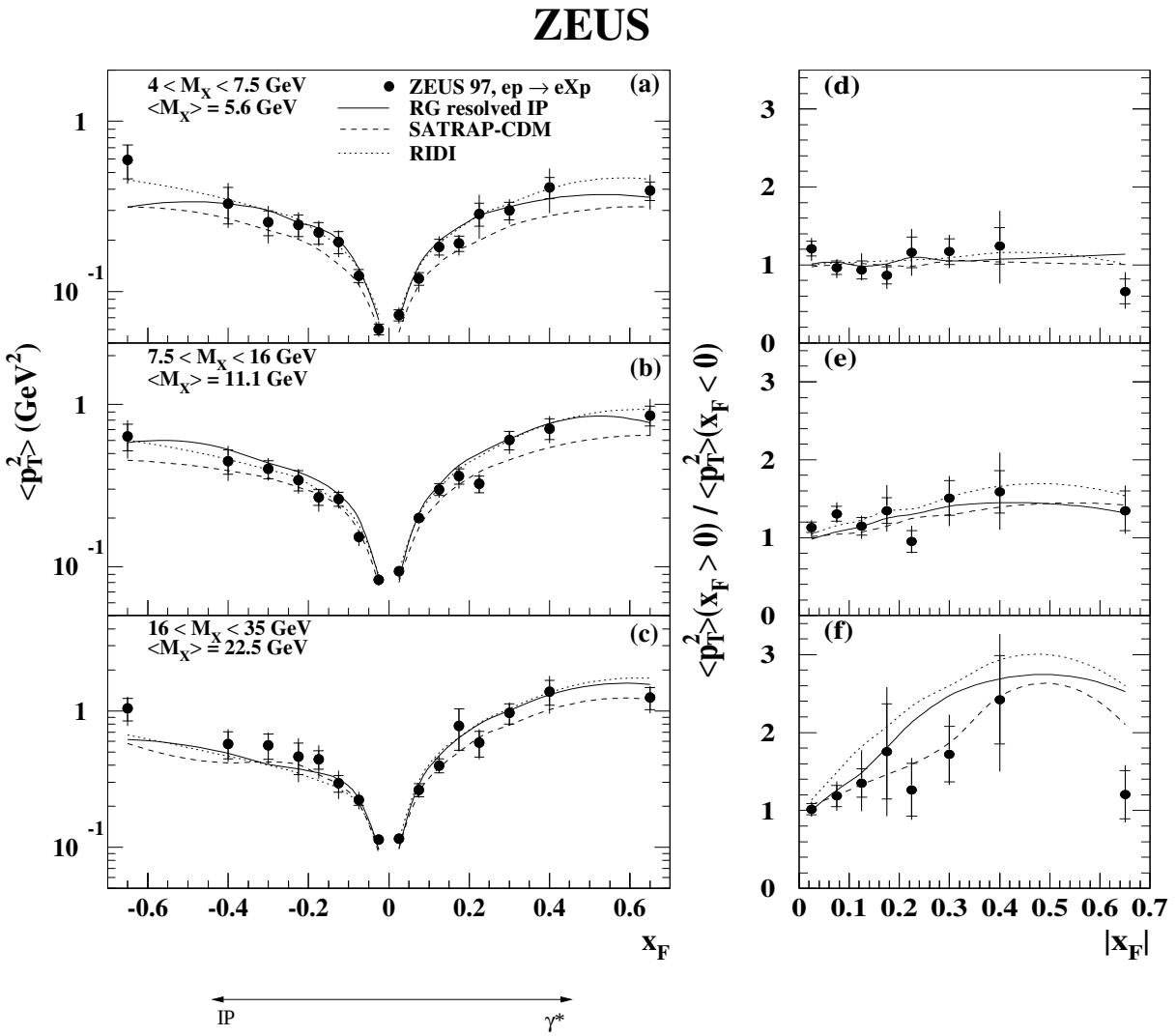

Figure 14: *Average squared transverse momentum as a function of x_F (seagull plot) in three bins of M_X in the $\gamma^*\mathbb{P}$-CMS (a-c) and the ratios of average momenta in the γ^* and $\mathbb{P}$ hemisphere as function of $|x_F|$ (d-f). The data (points) are compared to three models: RAPGAP (solid curve), SATRAP-CDM (dashed curve), and RIDI (dotted curve). Positive x_F is in the direction of the virtual photon. The inner error bars show statistical uncertainties only; the outer bars show the statistical and systematic uncertainties added in quadrature.*